Journal of Anatomy

J. Anat. (2017) **231**, pp169–191 doi: 10.1111/joa.12625

Digital dissection of the model organism *Xenopus laevis* using contrast-enhanced computed tomography

Laura B. Porro and Christopher T. Richards

Structure and Motion Laboratory, Department of Comparative Biomedical Sciences, Royal Veterinary College, Hatfield, Hertfordshire, UK

Abstract

The African clawed frog, *Xenopus laevis*, is one of the most widely used model organisms in biological research. However, the most recent anatomical description of *X. laevis* was produced nearly a century ago. Compared with other anurans, pipid frogs – including *X. laevis* – exhibit numerous unusual morphological features; thus, anatomical descriptions of more 'typical' frogs do not detail many aspects of *X. laevis* skeletal and soft-tissue morphology. The relatively new method of using iodine-based agents to stain soft tissues prior to high-resolution X-ray imaging has several advantages over gross dissection, such as enabling dissection of very small and fragile specimens, and preserving the three-dimensional topology of anatomical structures. Here, we use contrast-enhanced computed tomography to produce a high-resolution three-dimensional digital dissection of a post-metamorphic *X. laevis* to successfully visualize: skeletal and muscular anatomy; the nervous, respiratory, digestive, excretory and reproductive systems; and the major sense organs. Our digital dissection updates and supplements previous anatomical descriptions of this key model organism, and we present the three-dimensional data as interactive portable document format (PDF) files that are easily accessible and freely available for research and educational purposes. The data presented here hold enormous potential for applications beyond descriptive purposes, particularly for biological researchers using this taxon as a model organism, comparative anatomy and biomechanical modelling.

Key words: 3D visualization; amphibians; anatomy; Anura; CT-scanning; frog; iodine-potassium iodide.

Introduction

The African clawed frog, *Xenopus laevis* Daudin, 1802, is one of the most widely used organisms in biological research, including applications in cell and molecular biology, genetics, physiology, embryology, development and morphogenesis, neuroscience, biomechanics, toxicology and medicine (Gurdon et al. 1971; Gurdon & Hopwood, 2000; Burggren & Warburton, 2007; Wheeler & Brändli, 2009; Harland & Grainger, 2011; Cline & Kelly, 2012; Clemente & Richards, 2013; Richards & Clemente, 2013; Robovská-Havelková et al. 2014; Burgess, 2016). *Xenopus laevis* is easy to house and maintain, and its eggs and embryos are large, tolerate manipulation and are produced in large quantities (Wheeler & Brändli, 2009). The closely-related *Xenopus tropicalis* was the first amphibian to have its genome fully sequenced (Hellsten et al. 2010), and *X. laevis* was the first vertebrate to be successfully cloned (Gurdon et al. 1958). Recently, the tetraploid genome of *X. laevis* was successfully sequenced (Session et al. 2016), making *X. laevis* one of the most valuable model organisms for testing complex biological hypotheses.

Surprisingly, given the ubiquitous use and importance in biological research of *X. laevis*, its anatomy is incompletely known. The most recent monographical description of *X. laevis* was nearly a century ago (Grobbelaar, 1924). Subsequently, certain anatomical regions have been described in varying levels of detail, including: the pelvic and proximal hind limb skeleton and musculature (Green, 1931; Dunlap, 1960; Palmer, 1960; Emerson, 1982; Van Dijk, 2002; Ročkova & Roček, 2005; Přikryl et al. 2009); the pectoral skeleton (Robovská-Havelková, 2010); the abdominal wall (Ryke, 1953); and the head skeleton and musculature (Paterson, 1939; Trueb & Hanken, 1992; Roček, 1993; Smirnov, 1994; Hass, 2001; Ziermann & Olsson, 2007; Gross & Hanken, 2008; Ziermann & Diogo, 2014), particularly with regards to development. Excellent dissection guides for frogs are available (Minkoff, 1975), including the classic work by Ecker (1889) that uses several species of the neobatrachid *Rana* as the basis for anuran anatomy. However, members of the family

Correspondence
Laura B. Porro, Structure and Motion Laboratory, Department of Comparative Biomedical Sciences, Royal Veterinary College, Hatfield, Hertfordshire AL9 7TA, UK. E: lporro@rvc.ac.uk

Accepted for publication *15 March 2017*
Article published online *26 May 2017*

© 2017 Anatomical Society

Pipidae (including *X. laevis*), which occupy a basal position within Anura (Pyron & Wiens, 2011), exhibit a secondarily aquatic adult lifestyle and numerous autapomorphies compared with other anurans (Cannatella & Trueb, 1988; Cannatella & de Sá, 1993), including loss of the tongue and vocal cords, retention of the lateral line and greatly enlarged otic capsules, among many others (discussed below). Thus, anatomical descriptions of more 'typical' frogs do not detail many aspects of *X. laevis* skeletal and soft-tissue morphology. Additionally, the anatomical nomenclature used by Grobbelaar (1924) differs from the terminology used by Ecker (1889) and other more recent publications.

Despite the vast utility of gross dissection in understanding and teaching anatomy (and the frequent use of frogs to introduce students to dissection methods), this centuries-old practice is destructive and may be unsuitable for very small or delicate specimens. Recent methods employing radiographic contrast agents, particularly iodine-potassium iodide (I_2KI), alongside micro-computed tomography (μCT) permit visualization of soft tissues in high-resolution (Metscher, 2009a,b; Jeffery et al. 2011; Gignac et al. 2016). Diffusible iodine-based contrast-enhanced μCT (diceCT, *sensu* Gignac et al. 2016) has been used to produce digital dissections of many post-embryonic vertebrates, particularly the heads of fish (Metscher, 2013; Kleinteich et al. 2014; Brocklehurst, Porro et al. unpublished data), crocodilians (Tsai & Holliday, 2011; Holliday et al. 2013), birds (Düring et al. 2013; Lautenschlager et al. 2013; Quayle et al. 2014) and mammals (Cox & Jeffery, 2011; Hautier et al. 2012; Cox & Faulkes, 2014), as well as amphibian tongues (Kleinteich & Gorb, 2015a,b). Digital dissection via diceCT can be used to visualize very small or delicate soft-tissue structures, and structures deep to skeletal elements that are difficult to access via gross dissection. Simultaneously, diceCT precisely reveals the rich and intricate 3D topological relationships between the skeleton and soft-tissue structures. In addition to being used to illustrate anatomy for descriptive purposes, segmentation of these μCT datasets can be used to create interactive 3D reconstructions [including 3D portable document formats (PDFs)] that can be easily accessed by students and the general public. Finally, 3D reconstructions can be utilized by researchers interested in comparative anatomy, taxonomy and cladistics, and can serve as the basis for biomechanical analysis, including musculoskeletal modelling (Kargo et al. 2002) and finite element analysis (Holliday et al. 2013; Gignac et al. 2016).

We used diceCT to produce a high-resolution digital dissection of the model organism *X. laevis*, supplementing and updating previous descriptions. We focus on musculoskeletal anatomy, although our dissection also reveals the nervous, respiratory, digestive, excretory and reproductive systems, as well as the major sense organs. As in Holliday et al. (2013), we intend this contribution to serve as a visual atlas rather than a structure-by-structure verbal description of *Xenopus* anatomy, although we highlight features that differ radically in *X. laevis* compared with other frogs, and attempt to resolve discrepancies in the identification and nomenclature from previous publications. We emphasize that the 3D reconstruction (including its specific geometry) is our hypothesis regarding the anatomy of *X. laevis* and should be referred to for further details.

Materials and methods

A deceased post-metamorphic male specimen of *X. laevis* [snout–vent length (SVL): 18.38 mm; body mass (BM): 0.64 g] was obtained from an unrelated study and not collected for the purpose of this research; thus, animal care protocols are not required. The specimen was fixed in a 4% phosphate-buffered paraformaldehyde solution. All μCT-scanning was carried out at the Cambridge Biotomography Centre (Zoology Department) at the University of Cambridge in 2015 on an X-Tek H 225 μCT scanner (Nikon Metrology, Tring, UK). All specimens were scanned using a tungsten target, a background medium of air, no filter and were rendered as 16-bit TIFFs. The specimen of *X. laevis* was μCT-scanned prior to staining at 68 kV and 350 μA producing 1409 TIFF images at a resolution of 0.019 mm/voxel (Fig. 1A,C,E) – voxels were isometric for all scans. Subsequently, the specimen was stained in a solution of 3.75% weight-by-volume I_2KI for approximately 60 h; the solution was neither refreshed nor agitated during staining. Following staining, the specimen was μCT-scanned again at 72 kV and 290 μA producing 1490 TIFF images at a resolution of 0.017 mm/voxel (Fig. 1B,D,F). An unstained specimen of *Kassina maculata* (the red-legged running frog, SVL: 45.10 mm; BM: 13.68 g) was μCT-scanned at 65 kV and 340 μA producing 1158 TIFF images at a resolution of 0.0493 mm/voxel. *K. maculata* is a derived hyperoliid frog (nested within Neobatrachia and Ranoides; Pyron & Wiens, 2011) that thrives in varying terrain, and is capable of jumping, running, climbing and swimming (Ahn et al. 2004; Porro et al. 2017); this contrasts with the more basally positioned and almost exclusively aquatic *X. laevis*. Scan data from *K. maculata* were included to compare the unusual osteology of *X. laevis* with that of a taxon possessing a skeletal morphology and locomotor modes more typical of anurans.

Scan data were segmented in the visualization software Avizo 8.0 (FEI, Oregon, USA). Density thresholding was used to separate higher-density bone from lower-density soft-tissues in unstained datasets, and then processed slice-by-slice (interpolating across no more than five slices) to separate individual bones. The stained dataset of *X. laevis* was manually segmented to isolate individual soft tissues from each other. The dynamic histogram slider in Avizo was adjusted to enhance contrast between soft tissues. Anatomical structures were delineated using overall morphology, variations in density [e.g. nervous tissue was denser (brighter) than muscle, connective tissues separating muscles were less dense (darker) than surrounding muscle] and structural variations (e.g. differences in fibre orientation between adjacent muscles). Unstained and stained datasets of *X. laevis* were overlain using recognizable skeletal landmarks visible in both datasets and merged to create anatomical reconstructions. Three-dimensional surfaces were exported as wavefront (OBJ) files to create interactive 3D PDFs using Tetra4D Reviewer and Converter (Tech Soft 3D, Oregon, USA) and Adobe Acrobat Pro X (Adobe Systems, California, USA), following methods described by Lautenschlager & Ruecklin (2014). These reconstructions are provided as supporting information (Figs S1–S4) and are the basis for the following description.

© 2017 Anatomical Society

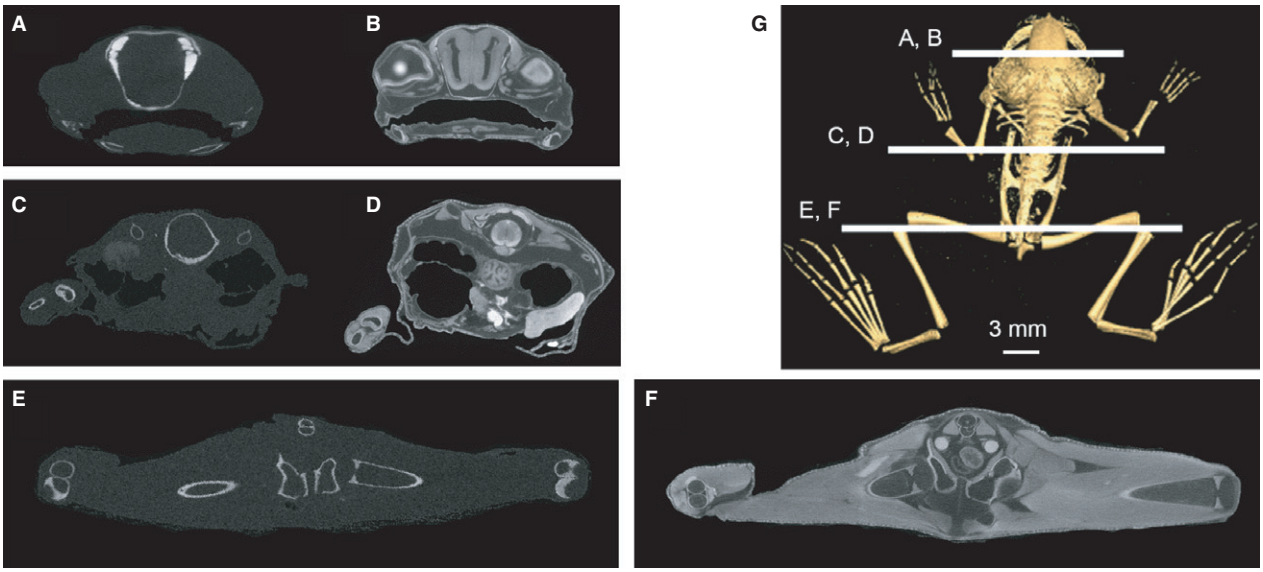

Fig. 1 Coronal/transverse micro-computed tomography (μCT) sections of *Xenopus laevis* specimen before (A,C,E) and after staining with I_2KI (B,D,F). Position of sections through the head (A,B), abdomen (C,D) and pelvis/hind limb (E,F) are shown in (G).

Results

Osteology

The skeletal anatomy of frogs, including *X. laevis*, has been extensively described (Ecker, 1889; Trueb & Hanken, 1992). Comparing the skull osteology of *X. laevis* and *K. maculata* (Fig. 2) highlights numerous autapomorphies of Pipidae, including: elongate septomaxillae; azygous frontoparietals; loss of the quadratojugal; flattening of the posterior and medial rami of the pterygoid; and loss of the mentomeckelian of the lower jaw (Cannatella & Trueb, 1988; Smirnov, 1994). The squamosal is modified into a funnel-shaped structure (unique to pipids) that houses the columnella, and its anterior process articulates with pterygoid (unique to *Xenopus* and *Silurana*). *Xenopus* is a neotenic frog in which development continues after sexual maturation (Smirnov, 1994). Our digital dissection of a young individual underscores features of *Xenopus* cranial morphology that vary during ontogeny. In our specimen: the nasals are separate (they fuse in older animals) while the vomers are azygous (they are paired in older animals); the palatine is absent (it appears in older individuals); the maxilla lacks a preorbital process and the parasphenoid lacks lateral alae (both appear in animals over 12 years old; Cannatella & Trueb, 1988; Smirnov, 1994).

Unusual features in the postcranial skeleton of *X. laevis* compared with neobatrachians (Figs 3 and S1) include fusion of the sacrum and urostyle, unique ridging on the ilia and urostyle, absence of the omosternum, fusion of the clavicle and scapula, and presence of a cartilaginous praepubis/epipubis (Cannatella & Trueb, 1988; Reilly & Jorgensen, 2011). Pronounced differences in pelvic morphology – including overall shape, and the nature of the sacroiliac and sacrourostylic articulations – among anuran taxa have been linked to divergent locomotor behaviours (e.g. predominantly swimming in *X. laevis*; Whiting, 1961; Emerson, 1979, 1982; Reilly & Jorgensen, 2011).

Musculature

Details of muscle origins and insertions are described in Table 1 and presented in Fig. S2.

Head and throat musculature

We use the nomenclature of Ziermann & Diogo (2014) to label and describe anuran head musculature; however, the terminology for the cranial muscles in anurans varies even among recent publications (Hass, 2001; Johnston, 2011). The orbital musculature (Fig. 4A–C) is composed of six extrinsic muscles: the four rectus muscles, which originate from the posteromedial corner of the orbit and surround the optic nerve (CN II); and the two obliquus muscles, which originate from the anteromedial corner of the orbit. The three portions of M. retractor bulbi are surrounded by the cone formed by the rectus muscles, and M. levator bulbi forms the floor of the orbital cavity (Fig. 4C). The jaw elevators (Fig. 4D–F) are identified by their attachment sites and relationships to the mandibular branch of the trigeminal nerve (CN V_3). Ziermann & Diogo (2014) divide M. adductor mandibulae A2 (identified in older publications as the masseter) into A2 and A2 lateralis portions; however, separate muscle bodies cannot be visualized in our μCT data. Fusion of M. adductor mandibulae A2 PVM (posteroventromesial) and A3′ creates the muscle widely known as the temporalis, which is separated from the deeper A3″ (pterygoideus) by

© 2017 Anatomical Society

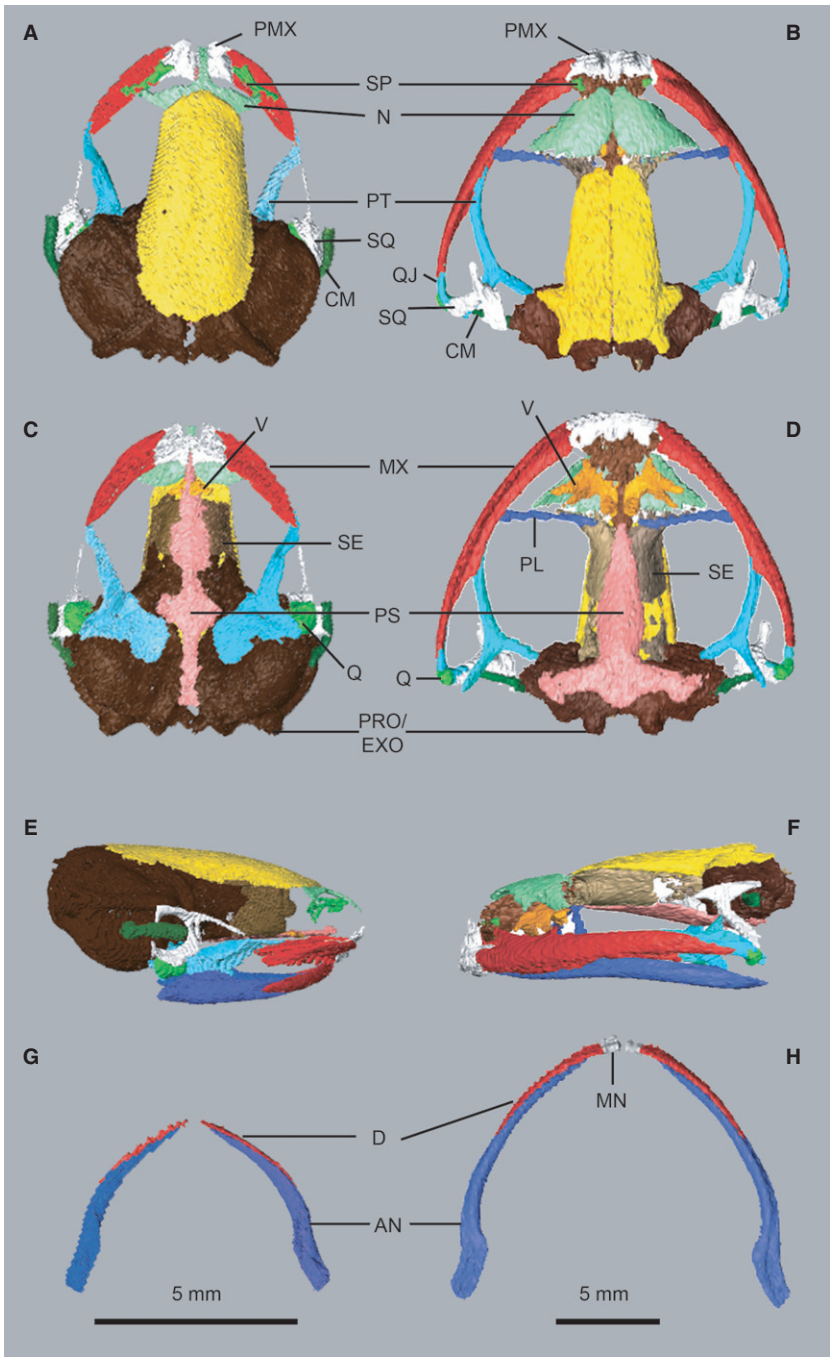

Fig. 2 Skull osteology of *Xenopus laevis* (A, C,E,G) and *Kassina maculata* (B,D,F,H). Crania (upper jaw) in dorsal (A,B) and ventral (C,D) views; skull and lower jaw in lateral view (E,F); lower jaw in dorsal view (G,H). AN, angulosplenial; CM, columnella; D, dentary; MN, mentomeckelian; MX, maxilla; N, nasal; PL, palatine; PMX, premaxilla; PRO/EXO, prootic-exoccipital; PS, parasphenoid; PT, pterygoid; Q, quadrate; QJ, quadratojugal; SE, sphenethmoid; SP, septomaxilla; SQ, squamosal; V, vomer.

CN V_3. A synapomorphy of Pipidae is the division of the M. depressor mandibulae, the primary jaw opener, into two parts (Cannatella & Trueb, 1988); the separate origins of the larger and smaller portions dorsal and ventral to M. cucullaris, respectively, are visible in our μCT data (Fig. 4E).

As *Xenopus* lacks a tongue, the hyoid musculature is highly unusual (Fig. 4G,H): M. hypoglossus, M. genioglossus (Grobbelaar, 1924; Ziermann & Diogo, 2014), and portions of M. petrohyoideus (see below) are absent. The M. intermandibularis anterior and posterior (widely known as the submentalis and submaxillaris/mylohyoideus, respectively) form the floor of the oral cavity and underlie all other throat muscles; a robust posterior slip of M. intermandibularis posterior originates on the ventral margin of the lateral edge of the pterygoid and anteroventral margin of the prootic, and is likely the muscle referred to as the M. subhyoideus by Grobbelaar (1924) and figured by Ecker (1889) (Fig. 4G). The paired M. geniohyoideus muscles are well developed, and each divides posteriorly into medial and lateral portions. M. sternohyoideus is an anterior continuation of M. rectus abdominus (see below); it originates external to M. rectus abdominis at the level of the clavicle (Ryke,

© 2017 Anatomical Society

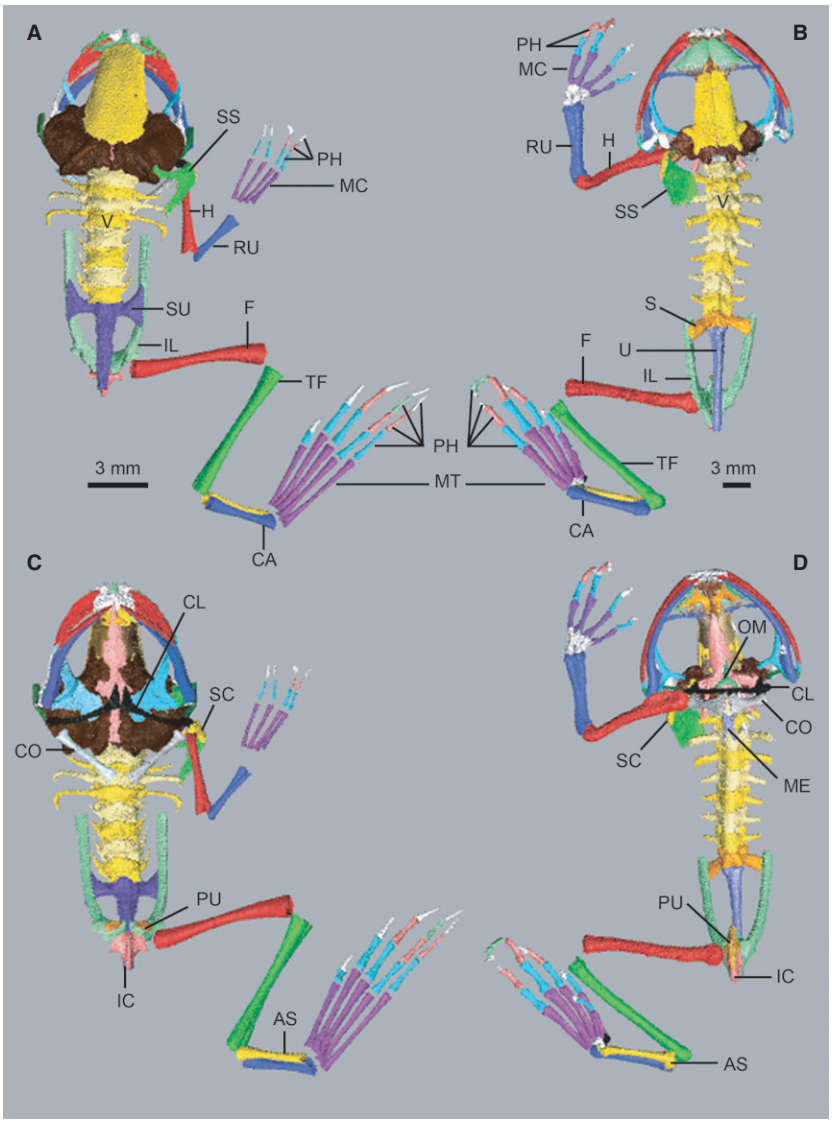

Fig. 3 Postcranial osteology of *Xenopus laevis* (A,C) and *Kassina maculata* (B,D) shown in dorsal (A,B) and ventral (C,D) views. AS, astragalus; CA, calcaneum; CL, clavicle; CO, coracoid; F, femur; H, humerus; IC, ischium; IL, ilium; MC, metacarpals; ME, mesosternum; MT, metatarsals; OM, omosternum; PH, phalanges; PU, pubis; RU, radioulna; S, sacral vertebrae; SC, scapula; SS, suprascapula; SU, fused sacrourostyle; TF, tibiofibula; U, urostyle; V, vertebrae.

1953), and is visible between the lateral and medial portions of M. geniohyoideus. The status of M. omohyoideus in *Xenopus* is unclear – Grobbelaar (1924) states this muscle is absent. In contrast, Ziermann & Diogo (2014) state M. omohyoideus is present in adult *Xenopus* and courses from the sternum to the hyoid; however, the typical origin of M. omohyoideus is on the anterior margin of the scapula (Ecker, 1889). An anterior slip of what we identify as M. sternoradialis may represent M. omohyoideus in our specimen. Frogs typically possess a single M. petrohyoideus anterior and three slips representing M. petrohyoideus posterior (Ecker, 1889); only one slip is present in *Xenopus* (Grobbelaar, 1924; Ziermann & Diogo, 2014), representing the posterior (third) slip of M. petrohyoideus posterior.

Back and abdominal musculature

Back muscles attaching to the pectoral girdle or forelimbs are discussed below. The back muscles of all frogs are externally (dorsally) covered by an extensive fascia dorsalis that attaches to the frontoparietal bone of the skull and spinous processes of the vertebrae (Ecker, 1889); in *Xenopus*, the posterior portion of fascia dorsalis thickens to become a ligamentous plate extending between the iliac shafts (Fig. 5A,E; Přikryl et al. 2009). The most prominent back muscle is M. longissimus dorsi, which extends from the anterior half of the urostyle to the occiput (Fig. 5A,D,E). M. coccygeosacralis is absent in *Xenopus* (Grobbelaar, 1924; Přikryl et al. 2009); M. coccygeoiliacus originates along the urostyle and passes ventral to the sacrum to insert on the medial aspect of the ilium (Fig. 5B,E). There are two origins for M. iliolumbaris as identified by Ryke (1953) and Palmer (1960)— the bulk of the muscle originates from the ventral aspects of the presacral vertebrae with one small slip originating on the tip of the transverse process of the 4th vertebra (Fig. 5B,D). Our digital dissection demonstrates M. iliolumbaris originates further anteriorly than previously described by some authors (but similar to Whiting, 1961), and may explain the extension of the iliac shafts far beyond

© 2017 Anatomical Society

Table 1 Origin and insertion sites for muscles in *Xenopus laevis*.

Muscle	Abbreviation	Origin	Insertion
Head and throat muscles			
M. rectus superior	RCS	Prootic, tendon from parasphenoid	Posterodorsal surface of eyeball
M. rectus inferior	RCI	Tendon from parasphenoid	Ventral surface of eyeball
M. rectus anterior (medialis)	RCA	Tendon from parasphenoid	Medial surface of eyeball
M. rectus posterior (lateralis)	RCP	Tendon from parasphenoid	Posteroventral surface of eyeball
M. obliquus superior	OBS	Parasphenoid	Dorsomedial surface of eyeball
M. obliquus inferior	OBI	Parasphenoid	Anteroventral surface of eyeball
M. retractor bulbi	RB′, RB″, RB‴	Parasphenoid	Posteroventral and posteromedial surfaces of eyeball
M. levator bulbi	LB	Frontoparietal, sphenethmoid	Pterygoid
M. adductor mandibulae A2 and A2 lateralis	A2	Anteroventral margin of the squamosal	Lateral aspect of the angulosplenial
M. adductor mandibulae A2 posteroventromesial + A3′	A3′	Lateral aspect of prootic-exoccpital, posterolateral margin of frontoparietal, dorsomedial aspect of anterior process of squamosal	Lateral aspect of coronoid process of the angulosplenial
M. adductor mandibulae A3″	A3″	Anterolateral aspect of prootic-exoccipital, lateral margin of frontoparietal	Dorsal margin of coronoid process of angulosplenial
M. depressor mandibulae	DM	Dorsal fascia and lateral aspect of prootic-exoccipital dorsal to stapes (outer part); posteroventral corner of squamosal and tympanic ring (inner part)	Posterodorsal tip of angulosplenial
M. intermandibularis anterior	IMA	Medial surface of anterior dentary	Same as origin
M. intermandibularis posterior	IMP	Dorsomedial surfaces of dentary, pterygoid/prootic	Midline raphe
M. geniohyoideus	GHY	Medial surface of anteriormost dentary	Hyoid bone and cartilage
M. sternohyoideus	SHY	Continuation of M. rectus abdominus	Hyoid bone and cartilage
M. petrohyoideus (posterior)	PHY	Prootic-exoccipital	Hyoid bone and cartilage
M. dilator laryngis	LAR	Cartilages of the larynx	Same as origin
Back and abdominal muscles			
M. longissimus dorsi	LGD	Spinous and transverse vertebral processes, occiput	Dorsal aspect of anterior half of urostyle
M. coccygeoiliacus	CGI	Lateral aspect of the urostyle	Medial surface of anterior third of ilium
M. iliolumbaris	IL	Lateroventral aspect of vertebrae 1–4, tip of transverse process of 4th vertebra	Lateroventral aspect of anterior tip of ilium
M. intertransversarii	ITR	Between adjacent transverse processes	Same as origin
M. intertransversarius capitis superior	ICS	Posterior aspect of prootic	Distal tip of transverse process of 2nd vertebra
M. intertransversarius captitis inferior	ICI	Posteroventral aspect of prootic	Distal tip of transverse process of 2nd vertebra
M. obliquus externus	OBE	Dorsal fascia, ligamentous plate	Ventral aponeurosis, linea alba
M. transversus abdominis	TRA	Dorsal fascia, ligamentous plate	Ventral aponeurosis, linea alba; sternum and pharynx
M. rectus abdominus superficialis	RAS	M. rectus abdominis profundus, linea alba	M. pectoralis, scapula
M. rectus abdominus profundus	RAP	Epipubis, linea alba	Clavicle, continuation of M. sternohyoideus
Pectoral and forelimb muscles			
M. cucullaris	CUL	Stapes, otic capsule and tympanic annulus	Medial aspect of anterior margin of supra scapula

(continued)

© 2017 Anatomical Society

Table 1 *(continued)*

Muscle	Abbreviation	Origin	Insertion
M. rhomboideus anterior	RBA	Posterodorsal aspect of exoccipital	Anterodorsal tip of suprascapula
M. levator scapulae superior	LSS	Lateral aspect of prootic-exoccipital	Medial aspect of posterodorsal suprascapula
M. levator scapulae inferior	LSI	Ventral aspect of prootic-exoccipital and parasphenoid	Medial aspect of posteroventral suprascapula
M. latissimus dorsi	LTD	Dorsal fascia	Dorsal surface of deltoid crest (tuberosity) of humerus
M. serratus superior	SRS	Dorsal fascia, distal tips of third and fourth vertebral processes	Dorsal margin of suprascapula
M. serratus medius	SRM	Distal tip of third transverse vertebral process	Medial aspect of suprascapula
M. serratus inferior	SRI	Distal tips of third and fourth transverse vertebral processes	Medial aspect of ventral suprascapula/ dorsal scapula
M. pectoralis (pars abdominalis)	PEC	Ventral fascia, linea alba, M. rectus abdominus	Ventral surface of deltoid crest of humerus
M. pectoralis (pars anterior sternalis)	PEC′	Ventral aspect of coracoid, sternal bones/cartilages	Ventral surface of deltoid crest of humerus
M. pectoralis (pars posterior sternalis)	PEC″	Posterior aspect of corocoid, sternal bones/cartilages	Ventral surface of deltoid crest of humerus
M. sternoradialis	STR	Sternal bones/cartilages, clavicle	Ventral/medial aspect of proximal radioulna
M. coracohumeralis	CRH	Coracoid and sternum	Humerus, adjacent to the deltoid crest
M. deltoideus	DEL	Lateral (external) aspect of scapula, lateral margin of clavicle, sternal bones/cartilages	Lateral aspect of distal humerus
M. interscapularis	ISC	Medial (internal) aspect of suprascapula	Medial (internal) aspect of scapula
M. subscapularis	SSC	Posterior margin of medial (internal) aspect of scapula	Ventral aspect of humerus
M. scapulo-humeralis profundus posterior	SHP	Posterior to glenoid of scapula	Dorsal aspect of proximal humerus
M. dorsalis scapulae	DSC	Lateral (external) aspect of ventral suprascapula	Dorsal surface of deltoid crest of humerus
Unknown pectoral girdle muscle	u	Dorsal aspect of distal tip of coracoid	Anteromedial aspect of scapula
M. triceps brachii (long head)	TRI	Posterior margin of scapula adjacent to glenoid	Tendon to proximal end of radioulna
M. triceps brachii [outer (lateral) head]	TRI′	Dorsal and lateral aspects of humerus	Tendon to proximal end of radioulna
M. triceps brachii [inner (medial) head]	TRI″	Ventral and medial aspects of humerus	Tendon to proximal end of radioulna
M. flexor carpi radialis	FCR	Medial aspect of distal humerus	Carpal bones
M. flexor carpi ulnaris	FCU	Medial aspect of distal humerus	Carpal bones
M. flexor digitorum communis	FDC	Medial aspect of distal humerus	Palmar aponeurosis of hand
M. flexor antebrachii medius	FAM	Medial aspect of distal humerus	Ventral surface of middle radioulna
M. flexor antebrachii lateralis superficialis	FALS	Medial epicondyle of humerus	Carpal bones and radioulna
M. flexor antebrachii lateralis profundus	FALP	Medial epicondyle of humerus	Radioulna
Pelvic and hind limb muscles			
M. iliacus externus outer layer	IE	Ventral aspect of ligamentous plate, dorsolateral aspect of middle iliac shaft	Anterodorsal aspect of proximal femur
M. iliacus externus middle layer	IE′	Lateral, dorsal and medial aspects of iliac shaft	Anterodorsal aspect of proximal femur, proximal to insertion of IE
M. iliacus externus middle layer (extra portion)	IE″	Ventral aspect of ligamentous plate, medial aspect of posterior iliac shaft	Same as M. iliacus externus middle layer

(continued)

© 2017 Anatomical Society

Table 1 *(continued)*

Muscle	Abbreviation	Origin	Insertion
M. iliacus externus deep layer	IE‴	Lateral, ventral and medial aspects of iliac shaft	Dorsal aspect of proximal femur, between insertions of outer and extra middle layers of M. iliacus externus
M. iliacus internus	II	Lateral, ventral and medial aspects of posterior iliac shaft	Anterodorsal aspect of femur, distal to IE insertions
M. pyriformis	PY	Dorsolateral aspect of mid urostyle	Dorsal aspect of femoral head
M. tensor fascia latae	TFL	Fascia covering ventral aspect of deep layer of M. iliacus externus	Fascia covering anterior aspect of M. cruralis
M. cruralis	CR	Ventrolateral aspect of ilium anteroventral to acetabulum	Knee aponeurosis
M. gluteaus magnus	GLM	Lateral aspect of dorsal process of ilium, anterior and dorsal to the origin of M. iliofibularis	Knee aponeurosis, fascia of M. cruralis
M. iliofemoralis	IFM	Lateral aspect of dorsal process of ilium, posterior and ventral to origin of M. iliofibularis	Along dorsal aspect of proximal half of femur
M. gracilis major	GMA	Lateral aspect of posterior ischial rim	Posterior aspect of medial tibiofibular head, distal to insertion of M. semitendinosus
M. gracilis minor	GMI	Posterolateral tip of ischium, wall of cloaca	Combined insertion with M. gracilis major
M. semimembranosus	SM	Lateral aspect of posterodorsal ischial rim	Posterior aspect of medial tibiofibular head
M. semitendinosus	ST	Lateral aspect of ventral ischial rim	Posterior aspect of medial tibiofibular head, distal to insertion of M. semimembranosus
M. sartorius	SA	Praepubis	Knee aponeurosis and medial aspect of tibiofibular head
M. adductor magnus dorsal head	ADD	Lateral aspect of ischial rim, deep to origin of M. gracilis major	Posterior aspect of proximal half of femur; dorsal and anterior aspects of distal half of femur
M. adductor magnus ventral head	ADV	Lateral aspect of ischial rim, anterior and ventral to origin of dorsal head of M. adductor magnus	Ventral aspect of femur
M. pectineus (and M. adductor longus)	PT-ADL	Lateral aspects of the anteroventral ilium and pubis	Ventral aspect of proximal femur
M. obturator externus (and M. quadratus femoris)	OBE-QF	Lateral aspect of dorsal ischium, surrounding acetabulum	Dorsal aspect of femoral head
M. obturator internus	OBI	Lateral aspect of ventral ischium, surrounding acetabulum	Ventral aspect of femoral head
M. gemellus	GML	Lateral aspect of posterodorsal ischial rim, between origins of M. semimebranosus and M. obturator externus	Posterodorsal aspect of proximal femur
M. iliofibularis	IFB	Lateral aspect of dorsal process of ilium, between origins of M. gluteus magnus and M. iliofemoralis	Posterodorsal aspect of lateral tibiofibular head via tendon
M. plantaris longus	PL	Knee aponeurosis, posterodorsal aspect of distal femur, posterolateral aspect of proximal tibiofibula	Plantaris tendon
M. peroneus	PE	Knee aponeurosis, anterolateral aspect of proximal tibiofibula	Anterolateral aspect of distal tibiofibula, lateral aspect of proximal head of the calcaneum
M. tibialis posticus	TBP	Posterior aspect of distal half of tibiofibula	Tendon to the astragalus

(continued)

© 2017 Anatomical Society

Table 1 *(continued)*

Muscle	Abbreviation	Origin	Insertion
M. tibialis anticus longus	TAL	Dorsal aspect of lateral femoral condyle	Anterolateral aspect of proximal head of the calcaneum, anteromedial aspect of proximal head of the astragalus
M. tibialis anticus brevis	TAB	Anterior and anteromedial aspects of the tibiofibula	Medial aspect of head of the astragalus
M. extensor cruris brevis	ECB	Knee aponeurosis	Anterior aspect of proximal tibiofibula
M. tarsalis anticus	TA	Anterolateral distal tibiofibula	Anteromedial aspect of astragalus
M. tarsalis posticus/ M. plantar profundus	TP/PP	Medial border of plantaris tendon	Posterior aspect of astragalus, tendon to prehallux, and plantar aponeurosis
M. flexor digitorum brevis superficialis	FDBS	Lateral border of plantaris tendon	Superficial flexor tendons to digits II–V
M. intertarsalis	IT	Lateral aspect of calcaneum and medial aspect of astragalus	Distal tarsal bones
M. extensor digitorum communis longus	EDCL	Lateral margin of M. tarsalis anticus	M. extensores breves
M. abductor brevis dorsalis digiti V	ABD 5	Anterior aspect of calcaneum	Lateral aspect of proximal metatarsal V
M. abductor brevis plantaris hallucis	ABPH	Lateral aspect of M. plantaris profundus	Ventral aspect of metatarsal I
M. lumbricales breves digitorum II–V, M. lumbricales longus digitiorum III–V and M. lumbricales longissimus digiti IV	LUM 2-5	Plantar tendon, superficial flexor tendons	Ventral surface of corresponding metatarso-digital joint, base of second phalanges of digits III–V, base of third phalanx of digit IV
M. interphalangeales digitorum III–V and M. interphalangealis distalis digiti IV	IPD	Ventral surface of proximal phalanx, and second phalanx of digit IV	Ventral surface of second phalanx, and third phalanx of digit IV
M. abductor brevis plantaris digiti V	ABP 5	Posterolateral tip of calcaneum	Lateroventral aspect of metatarsal V
M. extensor brevis superficialis hallucis	EBS 1	Anteromedial aspect of the calcaneum	Dorsolateral surface of metatarsal I and dorsal surface of proximal head of first phalanx of digit I
M. extensores breves superficiales digitorum II–IV	EBS 2–4	Medial aspect of distal calcaneum	Proximal heads of first phalanges of digits II – IV
M. extensor brevis medius digiti II	EBM 2	Lateral aspect of distal astragalus	Same as M. extensor brevis superficialis II
M. extensores breves profundii digitorum II–IV	EBP 2–4	Lateral and medial borders of metatarsi	Long tendons to distal phalanges
M. abductor brevis dorsalis hallucis	ABDH	Medial aspect of distal astragalus	Dorsomedial aspect of metatarsal I
Unknown foot muscle	u	Ventral aspect of metatarsal I	Ventral aspect of metatarsal I

the anterior margins of the sacrum (Ročkova & Roček, 2005). The M. intertransversarii between adjacent transverse processes are clear, but the M. intercrurales cannot be visualized in our specimen; however, Grobbelaar (1924) claims these two muscle masses are merged. Both M. intertransversarius capitis superior and inferior arise from the transverse process of the second vertebra and insert on the prootic-exoccpital complex (Fig. 5B).

In addition to work by Grobbelaar (1924), Ryke (1953) described the development of the trunk musculature of *Xenopus* during metamorphosis. M. obliquus externus is the most superficial abdominal muscle (although much of it is covered by M. latissimus dorsi and the abdominal portion of M. pectoralis; see Fig. 5A and below). A small slip representing pars scapularis of M. obliquus externus inserts between M. serratus inferior and M. latissimus dorsi; however, whether it ultimately inserts on the posterior margin of the scapula or suprascapula is unclear (Ecker, 1889; Grobbelaar, 1924; Ryke, 1953). The dorsal margin of M. transversus abdominis (which has merged with M. obliquus internus in frogs; Ecker, 1889) is externally overlapped by the ventral margin of M. obliquus externus;

© 2017 Anatomical Society

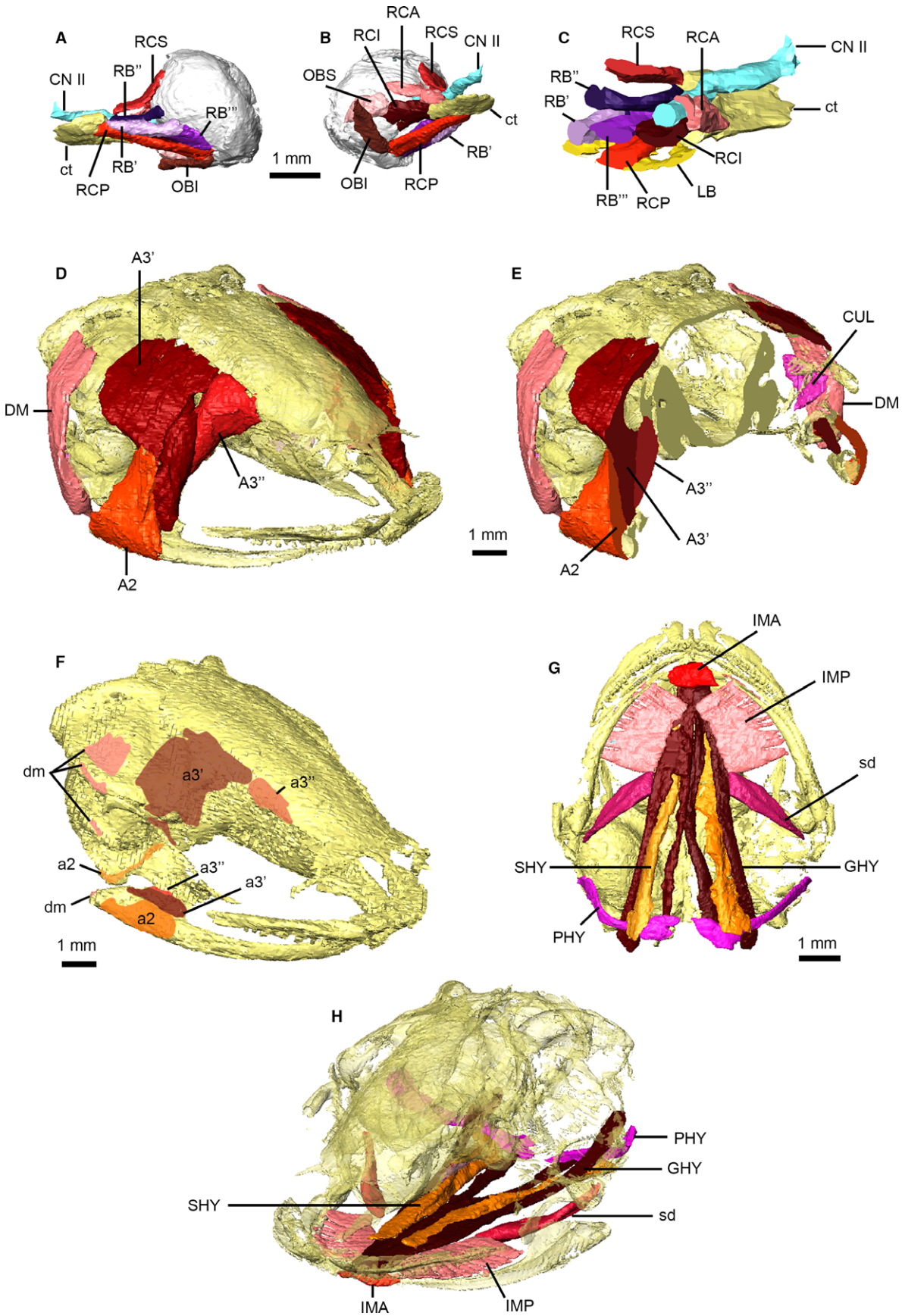

© 2017 Anatomical Society

Fig. 4 Head musculature of *Xenopus laevis*. Musculature of the right orbit in posterolateral (A) and posteromedial (B) views, and in transverse cross-section through the base of the eyeball (C). Jaw musculature in anterolateral view (D) and transverse cross-section through the coronoid process (E), and jaw muscle attachments on the skull upper and lower jaws (F). Hyoid musculature in ventral view (G) and posterior oblique view (H) with the skull transparent. Main muscle masses are identified using uppercase abbreviations; muscle attachment sites, small muscle slips and non-muscle structures are identified using lowercase abbreviations. A2, M. adductor mandibulae A2 (masseter); a2, attachments of A2; A3′, M. adductor mandibular A2 PVM and A3′ (temporalis); a3′, attachments of A3′; A3″, M. adductor mandibulae A3″ (pterygoideus); a3″, attachments of A3″; CN II, optic nerve; ct, central tendon; CUL, M. cucullaris; DM, M. depressor mandibulae; dm, attachments of DM; GHY, M. geniohyoideus; IMA, M. intermandibularis anterior; IMP, M. intermandibularis posterior; LB, M. levator bulbi; PHY, M. petrohyoideus posterior; OBI, M. obliquus inferior; OBS, M. obliquus superior; RB′/RB″/RB′″, portions of M. retractor bulbi; RCA, M. rectus anterior; RCI, M. rectus inferior; RCP, M. rectus posterior; RCS, M. rectus superior; sd, subhyoideus portion of IMP; SHY, M. sternohyoideus.

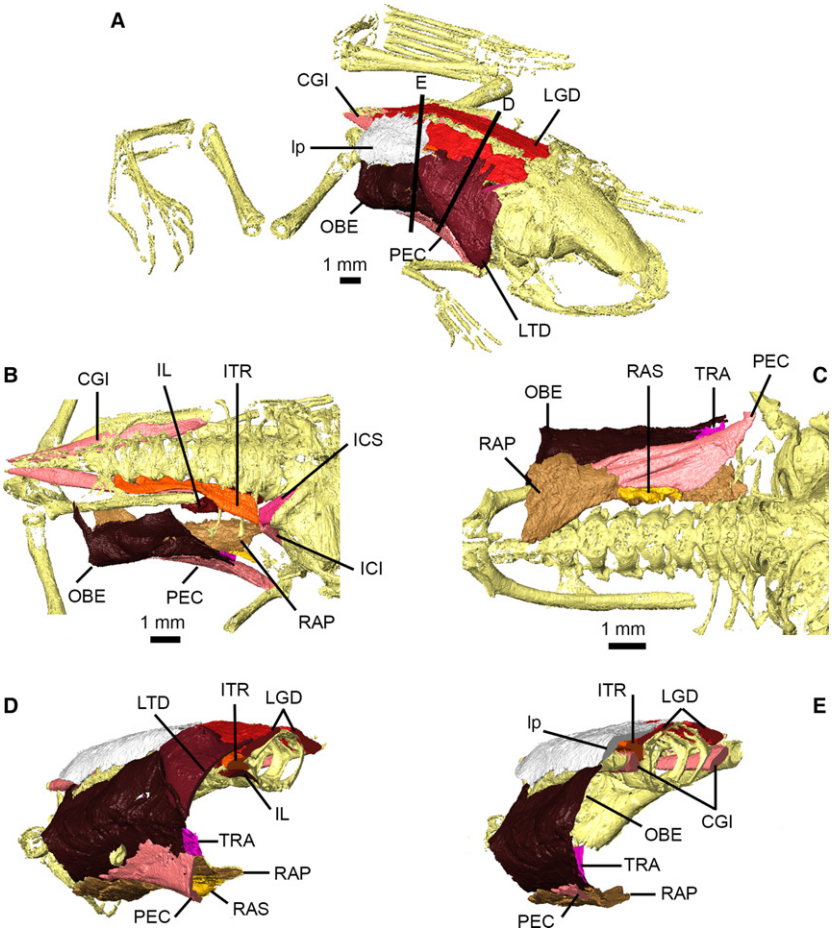

Fig. 5 Back and abdominal musculature of *Xenopus laevis*; both sides of M. longissimus dorsi and M. coccygeoiliacus are shown, otherwise only right side structures are depicted. Specimen shown in oblique view (A); dorsal view with ligamentous plate, M. longissimus dorsi and M. latissimus dorsi removed (B); ventral view (C); and transverse cross-sections (D,E) shown in (A). Muscles are identified using uppercase abbreviations; non-muscle structures are identified using lowercase abbreviations. CGI, M. coccygeoiliacus; ICI, M. intertransversarius capitis inferior; ICS, M. intertransversarius capitis superior; IL, M. iliolumbaris; ITR, M. intertransversarii; LGD, M. longissimus dorsi; lp, ligamentous plate; LTD, M. latissimus dorsi; OBE, M. obliquus externus; PEC, M. pectoralis pars abdominalis; RAP, M. rectus abdominus profundus; RAS, M. abdominus superficialis; TRA, M. transversus abdominus.

its anteroventral margin externally overlaps the dorsal margin of the deeper M. rectus abdominus (Fig. 5C–E). As noted by Ryke (1953), posterior portions of M. obliquus externus and M. transversus abdominus merge in post-metamorphic *Xenopus*, while the anteroventral fibres of M. transversus abdominis are indistinguishable from those of M. rectus abdominis profundus (Ecker, 1889; Ryke, 1953). The deep surface of M. transversus abdominis contacts several of the internal organs, particularly the lungs and liver (Ryke, 1953). M. rectus abdominis is divided into deep and superficial layers. M. rectus abdominis profundus forms the deepest layer of the abdominal musculature (Fig. 5C–E); it arises from the epipubis and longitudinally spans the ventral aspect of the abdomen on either side of the midline (Fig. 5C). Anteriorly, some fibres insert on the clavicle but most continue anteriorly as M. sternohyoideus. The posterior fibres of M. rectus abdominis superficialis in post-metamorphic *Xenopus* are indistinguishable from those of M. rectus abdominis profundus (Ryke, 1953). Anteriorly, its fibres follow and are closely associated with those of M. pectoralis (Fig. 5C), and insert on the scapula as described by Ecker (1889) and not on the sternum, contrary to descriptions by Grobbelaar (1924) and Ryke (1953).

Pectoral and forelimb musculature

As with the cranial musculature, the nomenclature for the muscles of the pectoral girdle and forelimb varies throughout the literature (Diogo & Ziermann, 2009). Several major

© 2017 Anatomical Society

pectoral muscles originate on the skull and vertebral column (Figs 5 and 6). The largest and most superficial of the dorsal pectoral muscles is M. latissimus dorsi (Figs 5A and 6A,G,H). *Xenopus* is unusual among anurans in that this muscle laterally overlaps the suprascapula and extends posteriorly to cover the anterior tips of the ilia (Grobbelaar, 1924; Přikryl et al. 2009). Mason et al. (2009) describe M. cucullaris as originating on the stapes, otic capsule and tympanic annulus in *X. laevis* (Fig. 6A,G), similar to descriptions and illustrations by Grobbelaar (1924) and Minkoff (1975); in contrast, Ecker (1889) describes and illustrates M. cucullaris arising from the posterodorsal aspect of the skull. This muscle is, in fact, M. rhomboideus anterior (Fig. 6A,G; Grobbelaar, 1924), and the muscle labelled and described as M. sternocleidomastoideus by Ecker (1889) is the M. cucullaris of Grobbelaar (1924) and Mason et al. (2009). Minkoff (1975) claims M. cucullaris and M. sternocleidomastoideus are synonymous; this appears to be the case as we could not identify a separate M. sternocleidomastoideus in our dataset. The M. levator scapulae superior (Fig. 6B,G,H) of later authors (Grobbelaar, 1924; Mason et al. 2009) appears to be equivalent to the M. protrahens scapulae of Ecker (1889), and the M. levator scapulae inferior (Fig. 6B,H) of Grobbelaar (1924) is equivalent to the M. levator anguli scapulae of Ecker (1889). The M. serratus superior, M. serratus medius and M. serratus inferior (Fig. 6C,H) of Grobbelaar (1924) are equivalent to the M. transverso-scapularis tertius s. serratus, M. transverso-scapularis minor and M. transverso-scapularis major, respectively, of Ecker (1889). Furthermore, Ecker (1889) describes an additional muscle (M. retrahens scapulae) with attachments identical to M. serratus inferior, and raises the possibility that the two may represent a single muscle; no separate M. retrahens scapulae was found in our specimen.

The ventral aspect of the posterior pectoral region is dominated by the M. pectoralis pars abdominalis (Figs 5C and 6D). M. pectoralis pars sternalis anterior and M. pectoralis pars sternalis posterior (Fig. 6D) of Ecker (1889) are equivalent to M. mylo-pectori-humeralis, M. supracoracoideus and M. sternocoracoideus of Grobbelaar (1924). The proximal portions of M. sternoradialis (M. coraco-radialis of Grobbelaar, 1924) and M. coracohumeralis (M. coraco-brachialis of Grobbelaar, 1924) are very difficult to separate in our dataset although their distal insertions on the forelimb are distinct (Fig. 6D,G). The M. scapulo-humeralis profundus anterior of Grobbelaar (1924) appears to be equivalent to M. subscapularis (Fig. 6E,H,J). However, our dataset reveals a small muscle that Grobbelaar (1924) terms the M. scapulo-humeralis profundus posterior; this muscle is either absent or microscopic in most anurans (Fig. 6E,G). The external surface of the shoulder is covered by M. dorsalis scapulae (M. infraspinatus of Grobbelaar, 1924), and three heads of M. triceps brachii (long, lateral and medial) are distinct in our scans (Fig. 6E,H–K); however, the fourth head [deep (Grobbelaar, 1924), anconeus (Minkoff, 1975), subanconeus (Ecker, 1889)] cannot be resolved in our dataset. An unknown muscle stretches between the internal aspect of the scapula and the distal tip of the coracoid (Fig. 6E).

Resolution of the flexor compartment muscles of the forearm is generally good (Fig. 6I–L), and M. flexor carpi radialis and ulnaris, M. flexor antebrachii medialis and M. flexor digitorum communis [M. palmaris longus of later studies (Minkoff, 1975)] are easily distinguished, although M. epitrochleocubitalis and M. ulnocarpalis cannot be resolved. In contrast, resolution of the muscles in the extensor compartment is poor and, with the exception of M. flexor antebrachii superficialis and profundus, individual muscles in this region and in the hand could not be distinguished due to the very small size of these structures. Attachment sites for pectoral and forelimb muscles are shown in Fig. 7.

Pelvic and hind limb musculature

The pelvic musculature of pipids, including *Xenopus*, is radically different from that of typical anurans (Figs 8 and 9). In addition to work by Grobbelaar (1924) and Dunlap (1960), the muscles of the pelvis and proximal hind limb of *Xenopus* have been more recently described by Přikryl et al. (2009). Dunlap (1960) described two portions of M. iliacus

Fig. 6 Pectoral and forelimb musculature of *Xenopus laevis*. Dorsal pectoral musculature shown in right dorsolateral view (A) with M. depressor mandibulae and M. latissimus dorsi transparent, right posterolateral view (B) with right suprascapula transparent, and right dorsolateral view (C) with suprascapula transparent. Ventral pectoral and arm musculature shown in ventral (D) and posterior (E) views. Dorsal view of specimen (F) detailing locations of transverse cross-sections through pectoral musculature (G,H). Arm and forearm musculature in dorsal (I) and ventral (J) views, and transverse cross-sections through the arm (K) and forearm (L), with sections shown in (I) and (J). Main muscles are identified using uppercase abbreviations; muscle slips and non-muscle structures are identified using lowercase abbreviations. CRH, M. coracohumeralis; CUL, M. cucullaris; DEL, M. deltoideus; DM, M. depressor mandibulae; DSC, M. dorsalis scapulae; FAM, M. flexor antebrachii medius; FALP, M. flexor antebrachii lateralis profundus; FALS, M. flexor antebrachii lateralis superficialis; FCR, M. flexor carpi radialis; FCU, M. flexor carpi ulnaris; FDC, M. flexor digitorum communis; ICI, M. intertransversarius capitis inferior; ICS, M. intertransversarius capitis superior; ISC, M. interscapularis; LGD, M. longissimus dorsi; LSI, M. levator scapulae inferior; LSS, M. levator scapulae superior; LTD, M. latissimus dorsi; PEC, M. pectoralis pars abdominalis; PEC′, M. pectoralis pars anterior sternalis; PEC″, M. pectoralis pars posterior sternalis; RBA, M. rhomboideus anterior; SHP, M. scapulo-humeralis profundus posterior; SRI, M. serratus inferior; SRM, M. serratus medius; SRS, M. serratus superior; SSC, M. subscapularis; STR, M. sternoradialis; tp, tympanic capsule; TRI, M. triceps brachii long head; TRI′, M. triceps brachii outer head; TRI″, M. triceps brachii inner head; u, unidentified pectoral girdle muscle.

© 2017 Anatomical Society

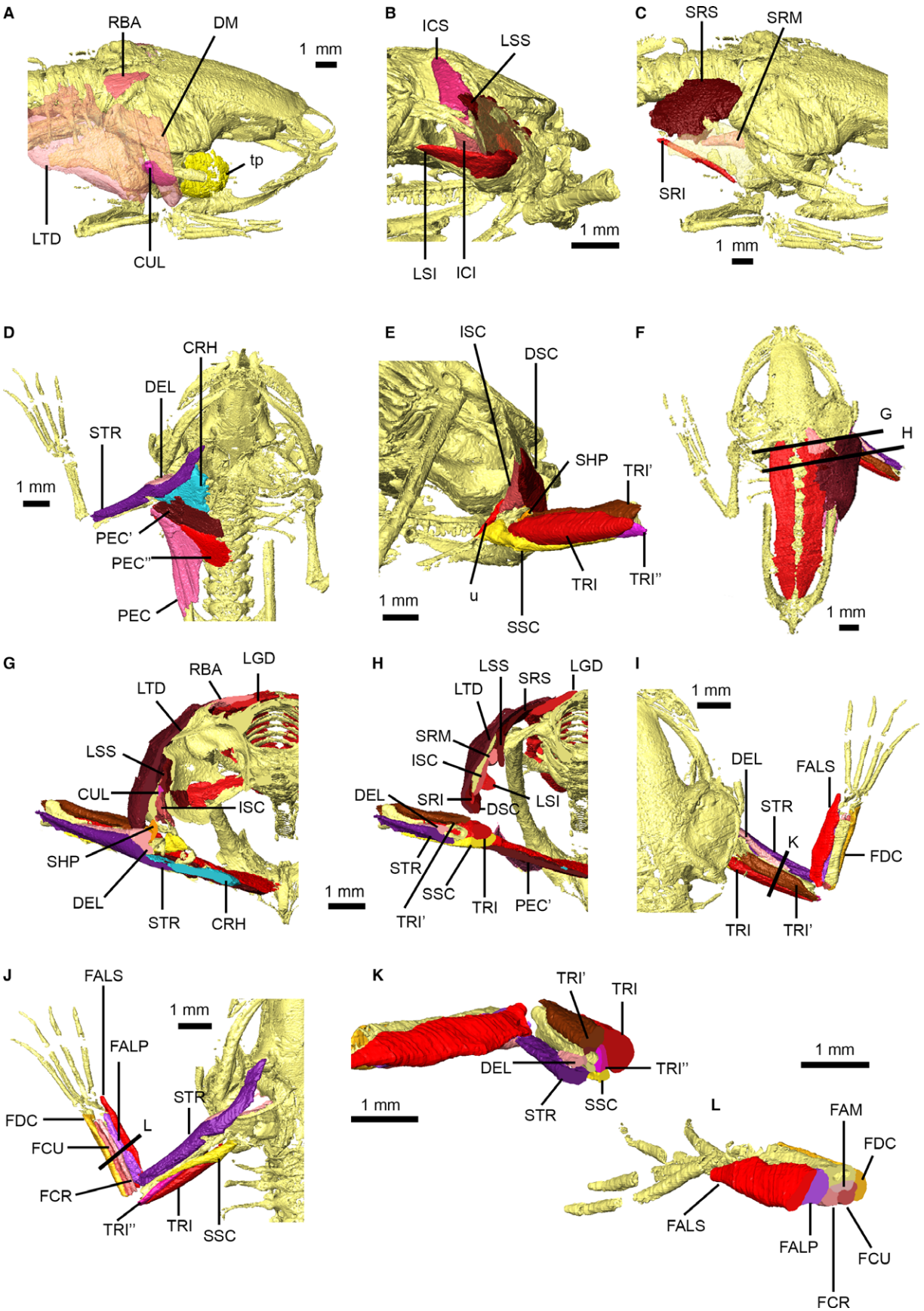

© 2017 Anatomical Society

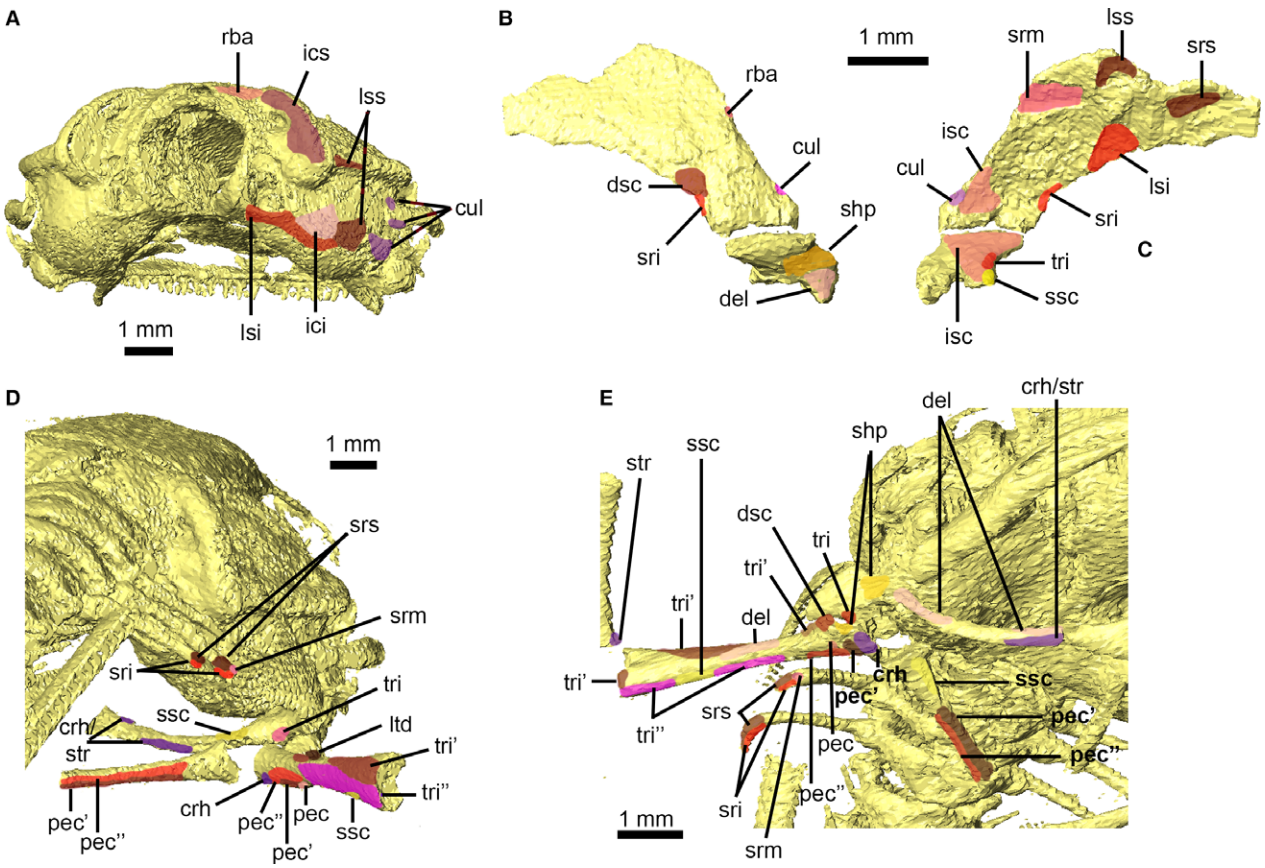

Fig. 7 Attachment sites for pectoral and forelimb musculature of *Xenopus laevis*. Skull shown in right posterolateral view (A). Right suprascapula and scapula shown in lateral (B) and medial (C) views. Close-up of pectoral and forelimb skeleton in right posterolateral view (D) and right ventrolateral view (E). Muscle attachment sites are identified using lowercase abbreviations. crh, attachment of M. coracohumeralis; cul, attachment of M. cucullaris; del, attachment of M. deltoideus; dsc, attachment of M. dorsalis scapulae; ici, attachment of M. intertransversarius capitis inferior; ics, attachment of M. intertransversarius capitis superior; isc, attachment of M. interscapularis; lsi, attachment of M. levator scapulae inferior; lss, attachment of M. levator scapulae superior; ltd, attachment of M. latissimus dorsi; pec, attachment of M. pectoralis pars abdominalis; pec′, attachment of M. pectoralis pars anterior sternalis; pec″, attachment of M. pectoralis pars posterior sternalis; rba, attachment of M. rhomboideus anterior; shp, attachment of M. scapulo-humeralis profundus posterior; sri, attachment of M. serratus inferior; srm, attachment of M. serratus medius; srs, attachment of M. serratus superior; ssc, attachment of M. subscapularis; str, attachment of M. sternoradialis; tri, attachment of M. triceps brachii long head; tri′, attachment of M. triceps brachii outer head; tri″, attachment of M. triceps brachii inner head.

externus in *Xenopus*; our digital dissection supports the presence of at least three separate layers (Fig. 8A,B,H–J), as described by Grobbelaar (1924), Ryke (1953) and Přikryl et al. (2009), although attachment sites vary slightly from those previously reported (Fig. 9). Additionally, our digital dissection revealed a distinct separate portion of the middle layer of M. iliacus externus (Figs 8A,B and 9B IE″) originating on the ventral surface of the ligamentous plate and medial aspect of the posterior iliac shaft, and sharing its insertion with the main middle portion of M. iliacus externus (IE′). In transverse cross-section, this muscle mass is what Ryke (1953, fig. 22) incorrectly labelled as M. coccygeosacralis, which is fused to M. longissimus dorsi in *Xenopus* (Přikryl et al. 2009). M. pyriformis is present and robust in our specimen (Fig. 8A) contra to suggestions by Dunlap (1960) and Přikryl et al. (2009) that it is reduced or absent. The M. epipubicus of Grobbelaar (1924), a muscle unique to *Xenopus*, could not be distinguished from the cartilaginous praepubis in our scan data.

The attachments of the thigh muscles of *X. laevis* are summarized in Table 1 and Fig. 9. Three thigh muscles – M. tensor fascia latae, M. cruralis and M. gluteus magnus – form what is known as the M. triceps femoris complex of frogs (Fig. 8C,D,J,K; Grobbelaar, 1924; Přikryl et al. 2009). The well-developed M. tensor fascia latae in our specimen has no bony attachments, originating from the fascia covering M. iliacus externus and inserting on the fascia of M. cruralis. Neither the division of M. cruralis into three heads nor the accessory tendon of M. gluteus magnus (Grobbelaar, 1924; Dunlap, 1960) can be visualized in our data. In contrast, the oblique tendinous inscriptions within M. semimembranosus and M. gracilis major are visible (Ecker, 1889; Přikryl et al. 2009). Although the anterior margin of M. semitendinosus and posterior margin of

© 2017 Anatomical Society

M. sartorius are closely associated in our datasets (Fig. 8D,I, J), both muscles are distinct and unfused, contra to descriptions by Grobbelaar (1924), Dunlap (1960) and Přikryl et al. (2009). Only the ventral head of M. semitendinosus is present in our specimen, as described and illustrated by Přikryl et al. (2009) for *X. laevis*. The ventral and dorsal portions of M. adductor magnus (Fig. 8E,F,I,J) are distinct and together form a muscular sheath (located between the superficial muscles of the thigh described above and the deepest layers, described below) that wraps around most of the femur. As noted by Dunlap (1960) and Přikryl et al. (2009), M. adductor longus is absent in *Xenopus* because it has not separated from M. pectineus (Fig. 8F,I); Grobbelaar (1924) describes the two muscles as being separate but in very close contact. Similarly, M. obturator externus is confluent with M. quadratus femoris in *Xenopus* (Fig. 8I; Grobbelaar, 1924; Dunlap, 1960; Přikryl et al. 2009).

The shank muscles of *X. laevis* (Fig. 10) have been described by Dunlap (1960), and were figured but not described by Grobbelaar (1924). The shank muscles are generally uniform across anurans (Dunlap, 1960). In contrast, numerous foot muscles present in most anurans are absent in *Xenopus*, including: M. abductor praehallucis; M. lumbricalis brevis hallucis; M. opponens hallucis; M. flexores ossei metatarsi digitorum III and IV; M. flexores teretes digitorum II and V; M. extensor brevis superficialis digiti V; and M. extensor brevis medius digiti IV. Within the shank, our μCT data reveal the fusion between the origins of M. peroneus and M. extensor cruris brevis characteristic of *Xenopus* as well as a heavy aponeourosis within M. plantaris longus (Fig. 10A,B). Resolution of individual muscles becomes difficult in the tarsus and foot due to the very small size of these structures. M. tarsalis posticus cannot be distinguished from M. plantaris profundus, with which it shares similar attachment sites (Fig. 10B,F,L). No distinction can be made between the M. lumbricales breves, longus and longissimus in our μCT data; the lumbricals (along with M. abductor proprius digiti IV) are presented in our digital dissection as a single, undivided mass (Fig. 10H). Furthermore, most of the very thin M. extensores breves medii digitorum are partially fused with M. extensores breves superficiales digitorum (Dunlap, 1960); only the muscle for the second digit is distinct in our dataset (Fig. 10G). Several very small foot muscles cannot be resolved in our data, including: the undivided M. transversus plantae; M. contrahentes digitorum I, II and V; M. flexor ossis metatarsi digiti II; M. flexores teretes digitorum III and IV; M. transversi metatarsi I–IV; and M. extensor brevis profundus digit V. Lastly, there is a substantial muscle along the ventral aspect of metatarsal I (Fig. 10H); the position of this muscle resembles those of the lumbricals in other digits. However, according to Dunlap (1960), M. lumbricalis brevis hallucis is absent in *Xenopus* and thus the identity of this muscle is uncertain.

Nervous system

Visualization of the central nervous system and the larger peripheral nerves in our dataset was excellent (Figs 11 and S3). The major portions of the brain – cerebral hemispheres, thalamencephalon/diencephalon, pineal body, optic lobes, hypothalamus and pituitary body, cerebellum and medulla oblongata, as well as their internal ventricles – are clearly visible (Fig. 11A–D). The olfactory lobes can be seen in surface renderings as anterolateral swellings of the cerebral hemispheres. There is no clear distinction between the medulla oblongata and spinal cord; in our reconstructions, the two are divided at the foramen magnum. The spinal cord features two prominent swellings along its length (Fig. 11E) from which arise the nerves of the pectoral and pelvic plexuses (Ecker, 1889). Posteriorly, the spinal cord tapers abruptly to a conus medullaris and filum terminale that continues into the urostyle (Fig. 11E).

There are 10 pairs of cranial nerves in frogs (Fig. 11E,F) – the accessory (CN XI) and hypoglossal (CN XII) nerves of amniotes are absent. The short olfactory nerve (CN I) courses from the anteroventral aspect of the olfactory lobe to the ventromedial aspect of the sphenethmoid cartilage (Fig. 11E).The optic nerves (CN II) can be traced from their chiasma on the ventral aspect of the brain to the eyes. The oculomotor nerve (CN III) can be traced emerging from the brain and passing through the wall of the cranium; it then passes near and exchanges fibres with the ophthalmic branch of the trigeminal nerve (CN V_1), becoming indistinguishable from the latter (Ecker, 1889). The trochlear nerve (CN IV), also closely associated with CN V_1 (Ecker, 1889), cannot be distinguished in our dataset. The largest cranial nerve, the trigeminal (CN V; Fig. 11F), arises from the anterolateral aspect of the medulla oblongata, passes forward to form the large Gasserian ganglion, then immediately divides into the ophthalmic branch (CN V_1) – which travels between the cranium and eyeball, before dividing into two terminal branches – and the maxillo-mandibular trunk. A large branch – the palatine nerve – originates near the base of CN V_1 and courses along the ventral aspect of the skull parallel to the midline. The maxillo-mandibular trunk passes behind the eyeball, between A3′ and A3″ and courses along the external surface of A3′ before dividing into the short maxillary branch (CN V_2) and longer mandibular branch (CN V_3). The tiny abducens nerve (CN VI) originates from the ventral aspect of the medulla oblongata behind the hypothalamus, joins the Gasserian ganglion and is then indistinguishable from CN V_1 (Fig. 11E). The facial nerve (CN VII) can be traced from the Gasserian ganglion, where it immediately divides into a short, stout palatal branch (that joins the palatine nerve of CN V_1) and a much longer hyomandibular branch, which courses posteriorly around the otic capsule, behind the angle of the lower jaw and then anteriorly along the ventral margin of the lower jaw. The auditory or vestibulocochlear nerve (CN VIII) is a

© 2017 Anatomical Society

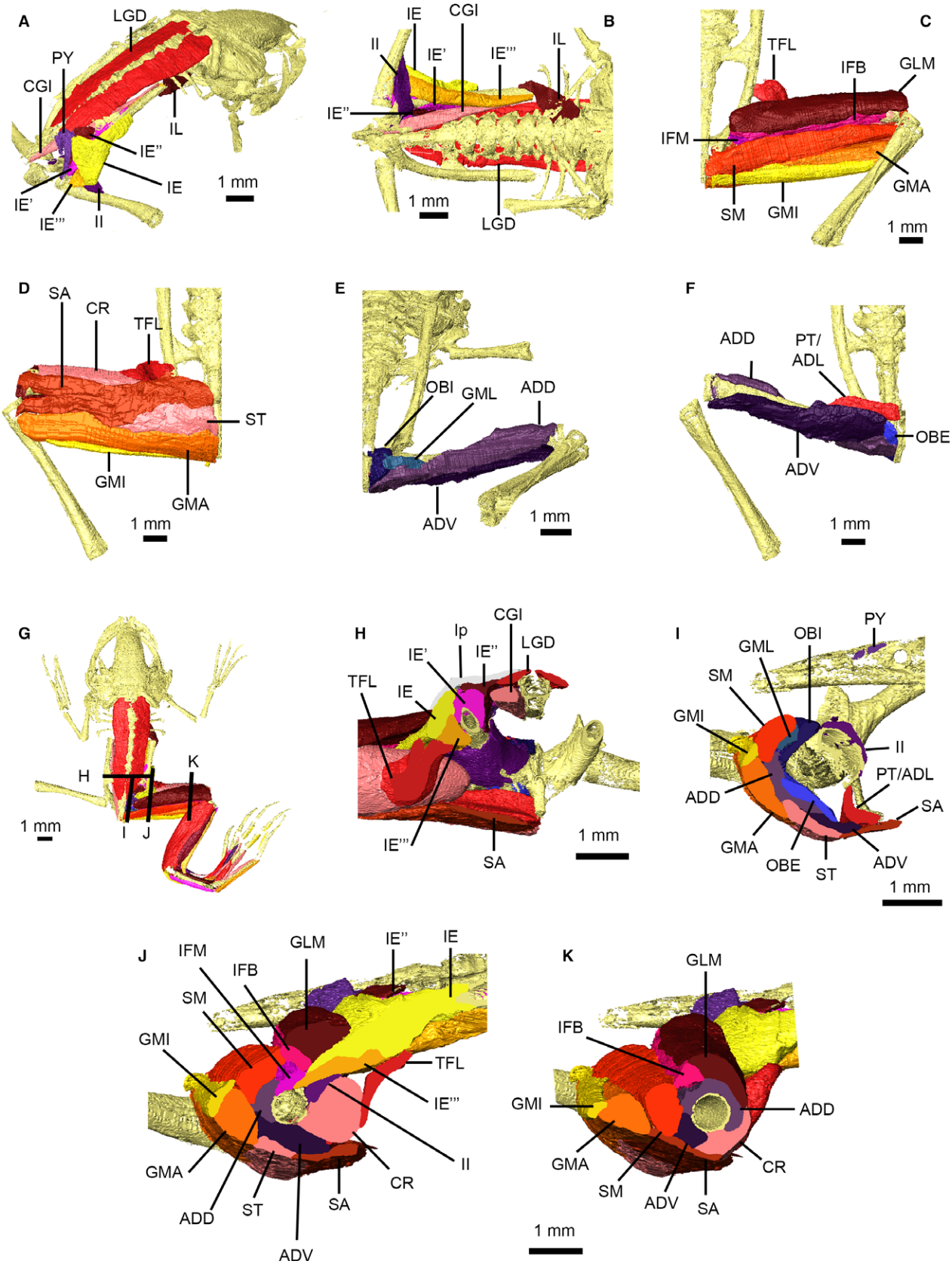

© 2017 Anatomical Society

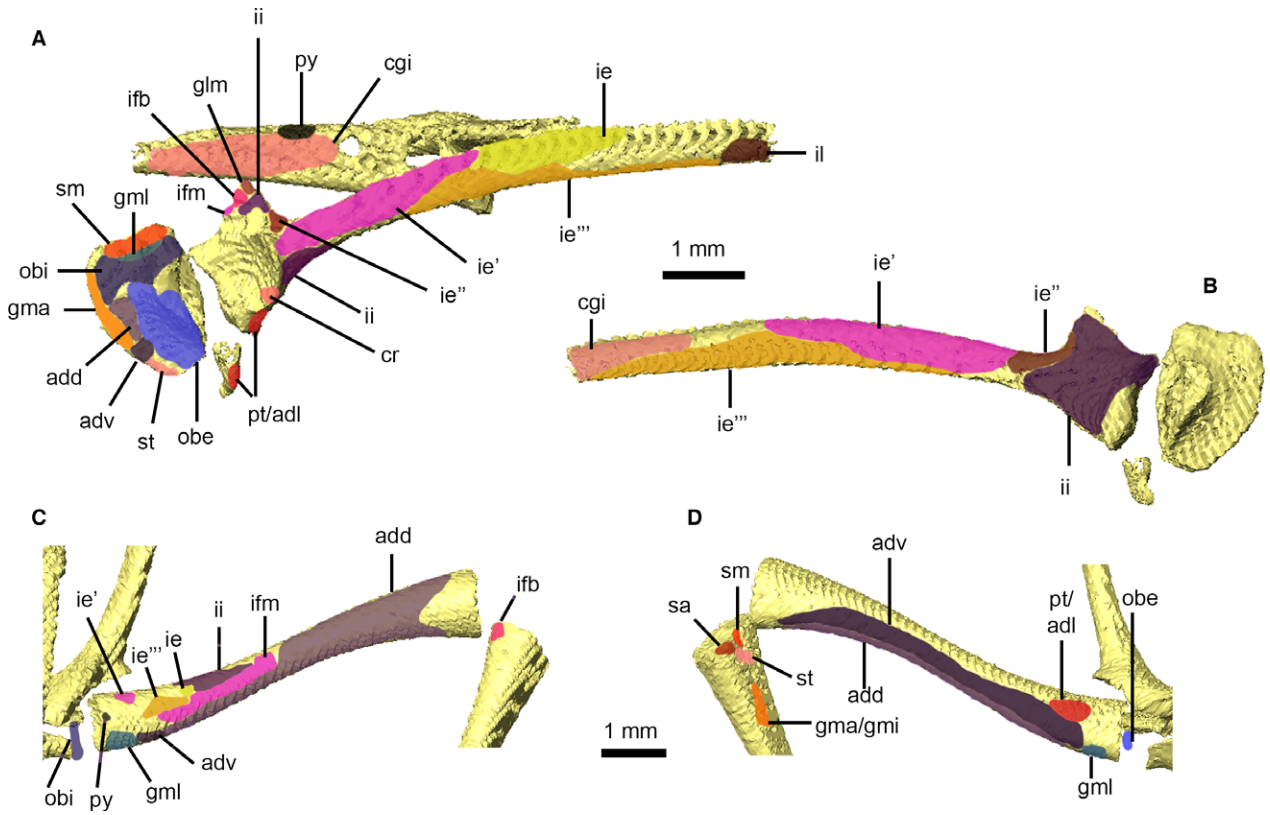

Fig. 9 Attachment sites for pelvic and thigh musculature of *Xenopus laevis*. Right ilium/pubis/ischium and urostyle in lateral view (A) and right ilium in medial view (B). Right femur in dorsal (C) and ventral (D) views. Muscle attachment sites are identified using lowercase abbreviations. add, attachment of M. adductor magnus, dorsal head; adl, attachment of M. adductor longus; adv, attachment of M. adductor magnus, ventral head; cgi, attachment of M. coccygeoiliacus; cr, attachment of M. cruralis; glm, attachment of M. glutaeus magnus; gma, attachment of M. gracilis major; gmi, attachment of M. gracilis minor; gml, attachment of M. gemellus; ie, attachment of M. iliacus externus, superficial layer; ie′, attachment of M. iliacus externus, middle layer; ie″, attachment of M. iliacus externus, extra middle layer; ie‴, attachment of M. iliacus externus, deep layer; ifb, attachment of M. iliofibularis; ifm, attachment of M. iliofemoralis; ii, attachment of M. iliacus internus; il, attachment of M. iliolumbaris; obe, attachment of M. obturator externus; obi, attachment of M. obturator internus; pt, attachment of M. pectineus; py, attachment of M. pyriformis; sa, attachment of M. sartorius; sm, attachment of M. semimembranosus; st, attachment of M. semitendinosus.

short, stout nerve that passes through a foramen into the otic capsule and immediately divides into a number of small nerves (Fig. 11E). The glossopharyngeal (CN IX) and vagus (CN X) nerves arise and exit the skull together, and cannot be differentiated in our dataset (although the former joins CN VII). CN X turns posteriorly and can be traced under the skin of the dorsolateral aspect of the back along the length of the body as it supplies the lateral line (Fig. 11E).

Ten pairs of spinal nerves were identified in our dataset (Fig. 11G); for each, the dorsal and ventral roots and spinal ganglia are clearly visible. Only major features of these nerves will be discussed here, as individual branches are detailed by Ecker (1889). The first spinal nerve [also called the hypoglossal nerve, Ecker (1889)] has an extremely slender dorsal root and emerges between the first and second vertebrae, giving off a series of small branches before

Fig. 8 Pelvic and thigh musculature of *Xenopus laevis*. Pelvic musculature in right dorsolateral (A) and ventral (B) views with the ligamentous plate removed. Superficial (C,D) and deep (E,F) thigh muscles in dorsal (C,E) and ventral (D,F) views. Dorsal view of specimen (G) showing location of cross-sections through the pelvis (H) and thigh (I–K). Muscles are identified using uppercase abbreviations; non-muscle structures are identified using lowercase abbreviations. ADD, M. adductor magnus, dorsal head; ADL, M. adductor longus; ADV, M. adductor magnus, ventral head; CGI, M. coccygeoiliacus; CR, M. cruralis; GLM, M. glutaeus magnus; GMA, M. gracilis major; GMI, M. gracilis minor; GML, M. gemellus; IE, M. iliacus externus, superficial layer; IE′, M. iliacus externus, middle layer; IE″, M. iliacus externus, extra middle layer; IE‴, M. iliacus externus, deep layer; IFB, M. iliofibularis; IFM, M. iliofemoralis; II, M. iliacus internus; IL, M. iliolumbaris; LGD, M. longissimus dorsi; lp, ligamentous plate; OBE, M. obturator externus; OBI, M. obturator internus; PT, M. pectineus; PY, M. pyriformis; SA, M. sartorius; SM, M. semimembranosus; ST, M. semitendinosus; TFL, M. tensor fascia latae.

© 2017 Anatomical Society

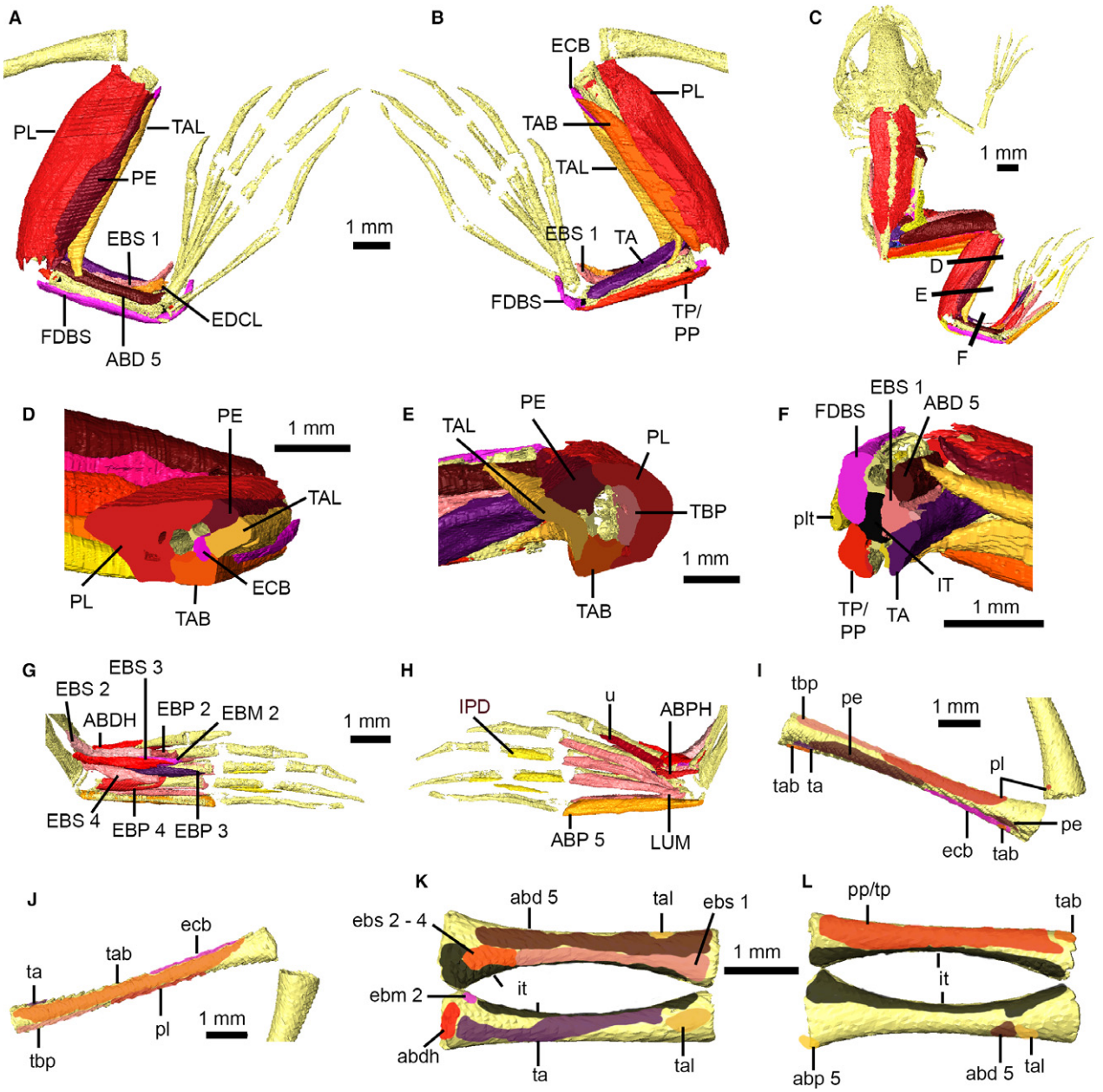

Fig. 10 Shank, tarsus and foot musculature of *Xenopus laevis*. Right shank and tarsal musculature in dorsal (A) and ventral (B) views. Dorsal view of specimen (C) showing location of cross-sections through the shank (D,E) and tarsus (F). Right foot musculature in dorsal (G) and ventral (H) views. Attachment sites on the right tibiofibula in dorsal (I) and ventral (J) views, and for the right tarsus in dorsal (K) and ventral (L) views. Main muscles are identified using uppercase abbreviations; muscle attachment sites and non-muscle structures are identified using lowercase abbreviations. ABD 5, M. abductor brevis dorsalis digiti V; abd 5, attachment of M. abductor brevis dorsalis digiti V; ABDH, M. abductor brevis dorsalis hallucis; abdh, attachment of M. abductor brevis dorsalis hallucis; ABP 5, M. abductor brevis plantaris digiti V; abp 5, attachment site of M. abductor brevis plantaris digiti V; ABPH, M. abductor brevis plantaris hallucis; EBM 2, M. extensor brevis medius digiti II; ebm 2, attachment of M. extensor brevis medius digiti II; EBP 2–4, M. extensor brevis profundus digiti II–IV; EBS 1, M. extensor brevis superficialis hallucis; ebs 1, attachment of M. extensor brevis superficialis hallucis; EBS 2–4, M. extensor brevis superficialis digiti II–IV; ebs 2–4, attachment of M. extensor brevis superficialis digiti II–IV; ECD, M. extensor cruris brevis; ecd, attachment of M. extensor cruris brevis; EDCL, M. extensor digitorum communis longus; FDBS, M. flexor digitorum brevis superficialis; IPD, M. interphalageales digitorum III–V; IT, M. intertarsalis; it, attachment of M. intertarsalis; LUM, M. lumbricales; PE, M. peroneus; pe, attachment of M. peroneus; PL, M. plantaris longus; pl, attachment of M. plantaris longus; plt, plantaris tendon; PP, M. plantaris profundus; pp, attachment of M. plantaris profundus; TA, M. tarsalis anticus; ta, attachment of M. tarsalis anticus; TAB, M. tibialis anticus brevis; tab, attachment of M. tibialis anticus brevis; TAL, M. tibialis anticus longus; tal, attachment of M. tibialis anticus longus; TBP, M. tibialis posticus; tbp, attachment of M. tibialis posticus; TP, M. tarsalis posticus; tp, attachment of M. tarsalis posticus; u, unknown foot muscle.

© 2017 Anatomical Society

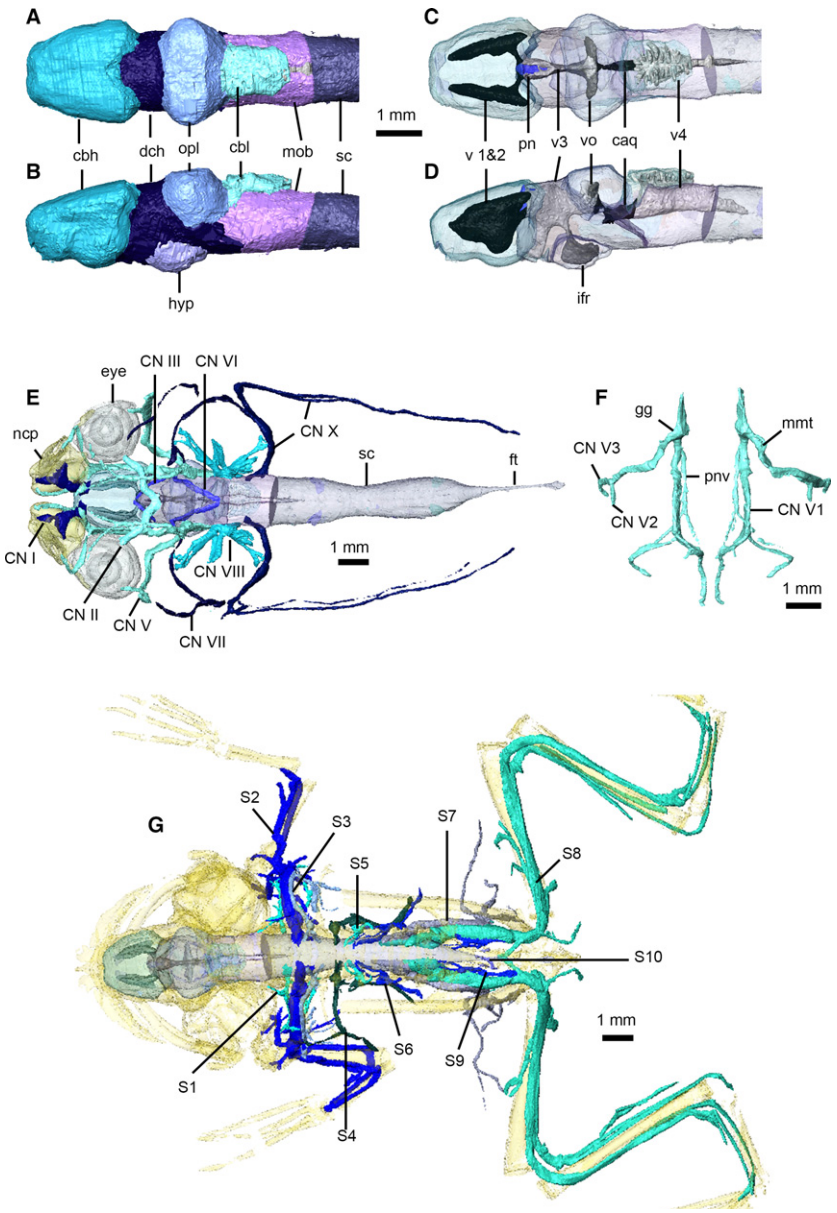

Fig. 11 Nervous system of *Xenopus laevis*. Brain in dorsal (A,C) and left lateral (B,D) views, with brain transparent in (C) and (D) to illustrate internal ventricles and pineal body. Cranial nerves in dorsal view (E), with eyes, nasal capsules, brain and spinal cord transparent. Left and right trigeminal nerves (F) in dorsal view. Peripheral nervous system in dorsal view (G), with brain, spinal cord and skeleton transparent (cranial nerves not shown). caq, cerebral aqueduct; cbl, cerebellum; cbh, cerebral hemispheres; CN I–X, cranial nerves 1–10; dch, diencephalon; ft, filum terminale; gg, Gasserian ganglion; hyp, hypothalamus; ifr, infundibular recess; mmt, maxilla-mandibular trunk; mob, medulla oblongata; ncp, nasal capsules; opl, optic lobes; pn, pineal body; pnv, palatine nerve; S 1–10, spinal nerves 1–10; sc, spinal cord; v 1 and 2, first and second ventricles; v3, third ventricle; v4, fourth ventricle; vo, optic ventricles.

turning sharply ventrally and anteriorly. The second spinal nerve is the large brachial nerve that supplies the shoulder and forelimb. The third spinal nerve is much smaller and, upon exiting between the third and fourth vertebrae, almost immediately joins the brachial nerve to supply the forelimb. The fourth, fifth and sixth spinal nerves are closely associated with each other and supply the abdominal muscles and skin. The seventh spinal nerve is large and initially follows the sciatic nerve before turning ventrally and medially, sending off a number of branches to the abdominal, pelvic and thigh muscles. The sciatic nerve is the largest nerve in the body and is composed primarily of the eighth and ninth spinal nerves, with contributions from the seventh; it supplies the hind limb. The 10th spinal nerve is extremely slender and exits the urostyle through a small lateral perforation.

Digestive system and glands

The digestive tract consists of the mouth, esophagus, stomach, small and large intestines, and their associated glands (Figs 12A,B and S4). *X. laevis* bears teeth on the premaxilla and maxilla, but vomerine teeth are absent in this species (Evans et al. 2015). The intermaxillary glands (Fig. 12A) are clearly visible between the anterior tip of the parasphenoid and the oral margin of the mouth, and the paired internal nares (choanae) open into the oral cavity immediately posterior to these glands. Further posteriorly, the left and right Eustachian tubes join and open into the pharynx via a single, median opening, a feature unique to pipids (Smirnov, 1994). The floor of the mouth in *X. laevis* is marked by the absence of a tongue.

© 2017 Anatomical Society

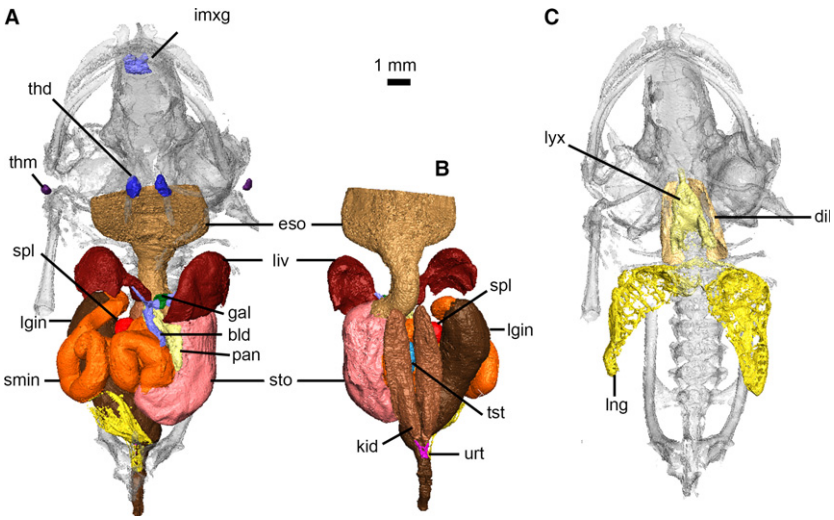

Fig. 12 Digestive, urogenital and respiratory systems of *Xenopus laevis*. Digestive and urogenital organs in ventral (A) and dorsal (B) views. Respiratory system in ventral view (C). bld, bile and cystic ducts; dil, M. dilator laryngis; eso, esophagus; gal, gallbladder; imxg, intermaxillary glands; kid, kidney; liv, liver; lgin, large intestine and rectum; lng, lung; lyx, larynx; pan, pancreas; smin, small intestine; spl, spleen; sto, stomach; thd, thyroid gland; thm, thymus gland; tst, testes; urt, ureter.

There is no clear distinction between the end of the oral cavity and the esophagus, which lies dorsal to the larynx. The esophagus (Fig. 12A,B) is a nearly straight tube that is largest (and dorsoventrally flattened) anteriorly and tapers to a rounded cross-section near its junction with the stomach. Scans reveal the tight folds of the mucosal and muscular layers of the esophagus becoming increasingly convoluted as it approaches the stomach. The junction between the esophagus and stomach is marked by a strong curve to the left, a marked increase in the diameter of the tube and noticeably thicker walls. The stomach (Fig. 12A,B) is kidney-shaped, and high-density particles visible within it (and the large intestine) in μCT scans are the remains of food. The stomach terminates by curving upwards and towards the right; a pronounced constriction marks the beginning of the long, coiling small intestine (Fig. 12A). Initially, the walls of the small intestine are thinner and exhibit less folding than those of the stomach. The walls become increasingly convoluted in the middle of the small intestine before once again thinning, with less pronounced folding as it approaches its junction with the large intestine. A sharp ventral curve and increase in diameter mark the beginning of the large intestine (Fig. 12A,B), which is initially very wide and thin-walled. The large intestine tapers abruptly as it passes between the ilia and ischia and opens into the cloaca dorsal to the opening of the bladder.

There are three distinct lobes of the liver, which occupy the anteroventral portion of the abdomen (Fig. 12A,B). All lobes are ventrally and anteriorly convex (domed) and dorsally concave. The left lobe is largest and covers the anteroventral surfaces of the stomach and left lung. The right lobe extends anterior to the left lobe, covers the anteroventral aspect of the right lung and is joined to the small median lobe, which lies posterior to the apex of the heart and overlaps the ventral aspect of the distal esophagus. The small, round gallbladder (Fig. 12A) lies between the left and median lobes, and is connected to the lobes of the liver by a series of hepatic and cystic ducts. The common bile duct from the gallbladder to the duodenum of the small intestine courses along the entire medial (right) border of the pancreas. The glandular pancreas (Fig. 12A) is flattened in cross-section and occupies a loop formed by the distal end of the esophagus, the stomach and the duodenum.

The spleen (part of the lymphatic system, but described here as an abdominal organ) is a radio-dense, small, round organ located on the right side of the abdomen within the curve formed by the large intestine and ventrally overlapped by the small intestine (Fig. 12A,B). The thymus glands (Fig. 12A) are small, circular bodies located on the sides of the head between M. depressor mandibulae and M. latissimus dorsi, and the oval-shaped thyroid glands (Fig. 12A) are located between the M. sternohyoideus and the anterior tip of the larynx.

Urogenital system

The paired kidneys (Figs 12B and S4) are elongate organs located ventral to the vertebrae and dorsal to the other abdominal organs, and extend from the fifth vertebra to the posterior end of the ilia. The ureters (Fig. 12B) are visible at the distal ends of the kidney. The urinary bladder (Fig. 12A) is bilobate (as in all amphibians), thin-walled and lies against the ventral aspect of the large intestine, opening into the cloaca ventral to the opening of the digestive tract. The individual we scanned possesses a pair of small, elongate organs located on the ventromedial aspect of the kidneys, approximately one-third from their anterior ends (Fig. 12B), which are testes and identify this young individual as a male. The adrenal glands could not be located and no fat bodies were present.

© 2017 Anatomical Society

Respiratory and circulatory systems

The respiratory tract consists of the larynx and lungs (Figs 12C and S4). The larynx is a funnel-shaped tube with its apex pointed anteriorly; it lies in the midline ventral to the esophagus, between the thyrohyals. The anterior end is a thin tapered tube that opens into the floor of the mouth via a longitudinal slit (glottis); posteriorly, a pair of short bronchi open into the lungs. The larynx is sexually dimorphic in *X. laevis*, and its shape in this specimen (as well as restriction of the M. dilator laryngis muscle to the lateral surfaces of the larynx) more closely resembles the female condition than that of the male (Sassoon & Kelley, 1986); this is due to the young age of this individual. The lungs are thin-walled and tear-drop shaped, tapering toward their posterior ends. They are located dorsal to the organs of the digestive tract and the left lung extends posteriorly beyond the right lung.

Although our methods produced excellent resolution of the muscles, internal organs and nervous system, visualization of the circulatory system was poor. The heart and the major vessels leading from the heart were over-stained, whereas the peripheral circulatory system did not stain. Little anatomical detail can be gleaned from the heart – it lies in the midline of the chest, with its apex resting near the median lobe of the liver. From surface renderings, the two atria and single ventricle can be identified. Excellent descriptions of the circulatory system of frogs (Ecker, 1889) and of *X. laevis* specifically (Grobbelaar, 1924) are available in the literature.

Discussion and conclusions

In this paper, we characterize the musculoskeletal, nervous, respiratory, digestive and urogenital anatomy of the key model organism *X. laevis* for the first time in nearly a century. We highlight the many unusual and unique morphological features of *X. laevis* (and pipids) compared with other frogs, and attempt to resolve discrepancies in the identification and nomenclature of various anatomical structures present in earlier publications. This was accomplished by utilizing the emerging technique of diceCT to visualize the 3D complex anatomy of *X. laevis*, the first such application of this method to produce a full-body digital dissection of any anuran. This technique was particular suitable in this instance due to the small size of the specimen and delicate nature of the anatomical structures. Furthermore, the method is non-destructive and replicable – our interpretation of the anatomy of *X. laevis* can be checked by other researchers through examination of original scan data. Lastly, this digital dissection preserves the 3D topological relationships of the anatomical structures and more comprehensively illustrates the anatomy of *X. laevis* than is possible in 2D media.

Application of diceCT to other anurans (and vertebrate clades) will permit researchers to bridge the gap between musculoskeletal anatomy and performance across macroevolutionary time scales. Following the pioneering work of Emerson (1979), Reilly & Jorgensen (2011) presented a new pattern for the evolution of pelvic bone morphology and locomotor mode in Anura. However, some skeletal features (e.g. iliac ridges) occurred across multiple locomotor modes, while some locomotor styles (e.g. arboreal jumpers) could not be diagnosed through skeletal characters. They suggested that other aspects of pelvic design and function – notably differences in pelvic and hind limb myology – needed to be compared across Anura to fully understand the evolution of locomotion in this clade. Our study takes a first step towards this – for example, our digital dissection demonstrates that the laterally directed iliac ridges of *X. laevis* serve as attachment sites for (from anterior to posterior): M. latissimus dorsi, the ligamentous plate, and the superficial and middle layers of M. iliacus externus. The unique, short T-shaped urostylic ridge serves as the attachment site for M. longissimus dorsi. Coupled with information on pelvic and hind limb kinematics and muscle activity during locomotion, we can now more fully understand the functional role of these osteological characters in living and fossil frogs. Furthermore, the ability to visualize nearly all soft tissues *in situ*, simultaneously and non-destructively makes it more likely that very delicate structures will not be overlooked (such as the two muscles we visualized but were unable to identify based on existing descriptions; see Results).

Our methods produced excellent resolution of the muscular anatomy – including identification of over 110 different muscles within our specimen – and particularly clear visualization of the nervous system. These results are presented in preceding illustrations as well as fully interactive 3D PDFs included as supplementary information. Some limitations to this study should be noted, including insufficient scan resolution to distinguish between the very smallest muscles of the foot and hand (see Results for details). Additionally, although our staining and scanning methods produced some visualization of the heart and of large, proximal circulatory vessels, it could not resolve the majority of the circulatory system. Alternative contrast-enhancing agents (such as BriteVu™) could be used to visualize arterial and vascular trees in 3D (Gignac et al. 2016). Furthermore, our methods did not permit visualization of muscle tendons (except those occurring inside muscles); using alternative contrast agents known to bind to collagen fibres could help visualize tendinous structures (Descamps et al. 2014) Lastly, this study details the anatomy of a young, post-metamorphic individual, and it is known that the morphology of *X. laevis* changes during growth; future anatomical studies of mature adults will permit detailed ontogenetic comparisons.

As showcased in this and other recent studies, diceCT provides a powerful new tool for anatomical research, able to produce detailed, anatomical atlases of key or rare living species for descriptive and educational purposes as well as 3D data suitable for further morphometric, biomechanical and taxonomic studies.

© 2017 Anatomical Society

Data accessibility

The primary dataset for this article is the 3D PDFs, which have been uploaded as part of the supplementary material; the reconstructions are available in other 3D formats upon request to the corresponding author.

Acknowledgements

The authors thank additional members of the team Amber J. Collings and Enrico Eberhard (Royal Veterinary College) as well as colleagues in the Structure and Motion Laboratory, particularly Emily Sparkes and Timothy West, for their support. Animal care and husbandry was provided by staff at the Biological Support Unit (RVC), with special thanks to Alastair Wallis. Advice on I_2KI staining was shared by Jen Bright (University of South Florida), Philip Cox (University of York), Paul Gignac (Oklahoma State University), Stephan Lautenschlager (University of Bristol) and Maedeh Borhani (Imperial College London). Robert Asher and Colin Shaw (University of Cambridge) provided access to CT-scanning facilities. Technical support for Avizo was provided by Alejandra Sánchez-Eróstegui and Jean Luc-Garnier (FEI Visualization Sciences Group). The authors have no competing interests.

Author contributions

LBP and RTC conceived of and designed the study; LBP carried out specimen staining and CT-scanning, reconstructed, segmented and interpreted the CT data, and created the 3D PDFs; LBP drafted the manuscript. Both authors gave final approval for publication.

Funding

This work was funded by a European Research Council (ERC) start grant ('PIPA 338271: Paleo-robotics and the innovations of propulsion in amphibians') to RTC.

References

Ahn AN, Furrow E, Biewener AA (2004) Walking and running in the red-legged running frog *Kassina maculata*. *J Exp Biol* **207**, 399–410.

Burgess S (2016) A matched set of frog sequences. *Nature* **538**, 320–321.

Burggren WW, Warburton S (2007) Amphibians as animal models for laboratory research in physiology. *ILAR J* **48**, 260–269.

Cannatella DC, de Sá RO (1993) *Xenopus* as a model organism. *Syst Biol* **42**, 476–507.

Cannatella DC, Trueb L (1988) Evolution of pipoid frogs: intergeneric relationships of the aquatic frog family Pipidae (Anura). *Zool J Linn Soc* **94**, 1–38.

Clemente CJ, Richards CT (2013) Muscle dynamics and hydrodynamics limit power and speed in swimming frogs. *Nat Commun* **4**, 2737.

Cline HT, Kelly BD (2012) *Xenopus* as an experimental system for developmental neuroscience: introduction to a special issue. *Dev Neurobiol* **72**, 463–464.

Cox PG, Faulkes CG (2014) Digital dissection of the masticatory muscles of the naked mole-rate, *Heterocephalus glaber* (Mammalia, Rodentia). *PeerJ* **2**, e448.

Cox PG, Jeffery N (2011) Reviewing the morphology of the jaw-closing musculature in squirrels, rats, and guinea pigs with contrast-enhanced micro-CT. *Anat Rec* **294**, 915–928.

Descamps E, Sochacka A, DeKegel B, et al. (2014) Soft tissue discrimination with contrast agents using micro-CT scanning. *Belg J Zool* **144**, 20–40.

Diogo R, Ziermann JM (2009) Development of fore- and hindlimb muscles in frogs: morphogenesis, homeotic transformations, digit reduction, and the forelimb-hindlimb enigma. *J Exp Zool B Mol Dev Evol* **322B**, 86–105.

Dunlap DG (1960) The comparative myology of the pelvic appendage in the Salientia. *J Morphol* **106**, 1–76.

Düring DN, Ziegler A, Thomason CK, et al. (2013) The songbird syrinx morpheme: a three-dimensional, high-resolution, interactive morphological map of the zebra finch vocal organ. *BMC Biol* **11**, 1.

Ecker A (1889) *The Anatomy of the Frog*. Oxford: Clarendon Press.

Emerson SB (1979) The ilio-sacral articulation in frogs: form and function. *Biol J Linn Soc* **11**, 153–168.

Emerson SB (1982) Frog postcranial morphology: identification of a functional complex. *Copeia* **3**, 603–613.

Evans BJ, Carter TF, Greenbaum E, et al. (2015) Genetics, morphology, advertisement calls, and historical records distinguish six new polyploid species of African clawed frog (*Xenopus*, Pipidae) from West and Central Africa. *PLoS One* **10**, e0142823.

Gignac PM, Kley NJ, Clarke JA, et al. (2016) Diffusible iodine-based contrast-enhanced computed tomography (diceCT): an emerging tool for rapid, high-resolution, 3D imaging of metazoan soft tissues. *J Anat* **228**, 889–909 doi: 10.1111/joa.12449.

Green TL (1931) On the pelvis of Anura: a study in adaptation and recapitulation. *Proc Zool Soc Lond* **101**, 1259–1290.

Grobbelaar CS (1924) Beiträge zu einer anatomischen Monographie von *Xenopus laevis* (Daud.). *Z Anat Entwicklungs* **72**, 131–168.

Gross JB, Hanken J (2008) Segmentation of the vertebrate skull: neural-crest derivation of adult cartilages in the clawed frog, *Xenopus laevis*. *Integ Comp Biol* **48**, 681–696.

Gurdon JB, Hopwood N (2000) The introduction of *Xenopus laevis* into developmental biology: of empire, pregnancy testing and ribosomal genes. *Int J Dev Biol* **44**, 43–50.

Gurdon JB, Elsdale TR, Fischberg M (1958) Sexually mature individuals of *Xenopus laevis* from the transplantation of single somatic nuclei. *Nature* **182**, 64–65.

Gurdon JB, Lane CD, Woodland HR, et al. (1971) Use of frog eggs and oocytes for the study of messenger RNA and its translation in living cells. *Nature* **233**, 177–182.

Harland RM, Grainger RM (2011) *Xenopus* research: metamorphosed by genetics and genomics. *Trends Genet* **27**, 507–515.

Hass A (2001) Mandibular arch musculature of anuran tadpoles, with comments on homologies of amphibian jaw muscles. *J Morphol* **247**, 1–33.

Hautier L, Lebrun R, Cox PG (2012) Patterns of covariation in the masticatory apparatus of hystricognahtus rodents: implications for evolution and diversification. *J Morphol* **273**, 1319–1337.

Hellsten U, Harland RM, Gilchrist MJ, et al. (2010) The genome of the western clawed frog *Xenopus tropicalis*. *Science* **328**, 633–636.

© 2017 Anatomical Society

Holliday CM, Tsai HP, Skiljan RJ, et al. (2013) A 3-D interactive model and atlas of the jaw musculature of *Alligator mississippiensis*. *PLoS One* **8**, e62806.

Jeffery NS, Stephenson RS, Gallagher JA, et al. (2011) Micro-computed tomography with iodine staining resolves the arrangement of muscle fibres. *J Biomech* **44**, 189–192.

Johnston P (2011) Cranial muscles of the anurans *Leiopelma hochstetteri* and *Ascaphus truei* and the homologies of the mandibular adductors in Lissamphibia and other gnathostomes. *J Morphol* **272**, 1492–1512.

Kargo WJ, Nelson F, Rome L (2002) Jumping in frogs: assessing the design of the skeletal system by anatomically realistic modeling and forward dynamic simulation. *J Exp Biol* **205**, 1683–1702.

Kleinteich T, Gorb SN (2015a) The diversity of sticky frog tongues. *Bruker microCT User Mtg Abstracts* **2015**, 1–4.

Kleinteich T, Gorb SN (2015b) Frog tongue acts as muscle-powered adhesive tape. *R Soc Open Sci* **2**, 150333.

Kleinteich T, Conway KW, Gorb SN, et al. (2014) What's inside a fish suction cup? *Bruker microCT User Mtg Abstracts* **2014**, 1–4.

Lautenschlager S, Ruecklin M (2014) Beyond the print – virtual paleontology in science publishing, outreach, and education. *J Paleontol* **88**, 727–734.

Lautenschlager S, Bright JA, Rayfield EJ (2013) Digital dissection – using contrast-enhanced computed tomography scanning to elucidate hard- and soft-tissue anatomy of the Common Buzzard *Buteo buteo*. *J Anat* **224**, 412–431.

Mason MJ, Wang M, Narins PM (2009) Structure and function of the middle ear apparatus of the aquatic frog, *Xenopus laevis*. *Proc Inst Acoust* **31**, 13–21.

Metscher BD (2009a) Micro-CT for comparative morphology: simple staining methods allow high-contrast 3D imaging of diverse non-mineralized animal tissues. *BMC Physiol* **9**, 11.

Metscher BD (2009b) Micro-CT for developmental biology: a versatile tool for high-contrast 3-D imaging. *Dev Dyn* **238**, 632–640.

Metscher BD (2013) Biological applications of X-ray microtomography: imaging micro-anatomy, molecular expression and organismal diversity. *Micrsosc Anal* **27**, 13–16.

Minkoff EC (1975) *A Laboratory Guide to Frog Anatomy*. New York: Pergamon Press.

Palmer M (1960) Expanded ilio-sacral joint in the toad *Xenopus laevis*. *Nature* **187**, 797–798.

Paterson NF (1939) The head of *Xenopus laevis*. *Q J Microsc Sci* **81**, 161–234.

Porro LB, Collings AC, Eberhard E, et al. (2017) Inverse dynamic modelling of jumping in the red-legged running frog *Kassina maculata*. *J Exp Biol* **10**, 1882–1893 doi: 10.1242/jeb.155416.

Přikryl T, Aerts P, Havelková P, et al. (2009) Pelvic and thigh musculature in frogs (Anura) and origin of anuran jumping locomotion. *J Anat* **214**, 100–139.

Pyron AR, Wiens JI (2011) A large-scale phylogeny of the Amphibia including over 2800 species, and a revised classification of extant frogs, salamanders, and caecilians. *Mol Phylogenet Evol* **61**, 543–583.

Quayle MR, Barnes DG, Kaluza OL, et al. (2014) An interactive three-dimensional approach to anatomical description – the jaw musculature of the Australian laughing kookaburra (*Dacelo novaeguineae*). *PeerJ* **2**, e355.

Reilly S, Jorgensen M (2011) The evolution of jumping in frogs: morphological evidence for the basal anuran locomotor condition and the radiation of locomotor systems in crown group anurans. *J Morphol* **272**, 149–168.

Richards CT, Clemente CJ (2013) Built for rowing: frog muscle is tuned to limb morphology to power swimming. *J R Soc Inter* **10**, 20130236.

Robovská-Havelková P (2010) How can ontogeny help us understand the morphology of the anuran pectoral girdle? *Zoomorphology* **129**, 121–132.

Robovská-Havelková P, Aerts P, Roček Z, et al. (2014) Do all frogs swim alike? The effect of ecological specialization on swimming kinematics in frogs. *J Exp Biol* **217**, 3637–3644.

Roček Z (1993) Origin and evolution of the anuran postnasal wall and adjacent parts of palatoquadrate. *Ethol Ecol Evol* **5**, 247–265.

Ročkova H, Roček Z (2005) Development of the pelvis and posterior part of the vertebral column in the Anura. *J Anat* **206**, 17–35.

Ryke PAJ (1953) The ontogenetic development of the somatic musculature of the trunk of the aglossal anuran *Xenopus laevis* (Daudin). *Acta Zool* **34**, 1–70.

Sassoon D, Kelley DB (1986) The sexually dimorphic larynx of *Xenopus laevis:* development and androgen regulation. *Am J Anat* **177**, 457–472.

Session AM, Uno Y, Kwon T, et al. (2016) Genome evolution in the allotetraploid frog *Xenopus laevis*. *Nature* **538**, 336–343.

Smirnov SV (1994) Postmaturation skull development in *Xenopus laevis* (Anura, Pipidae): late-appearing bones and their bearing on the pipid ancestral morphology. *Russ J Herpetol* **1**, 21–29.

Trueb L, Hanken J (1992) Skeletal development in *Xenopus laevis* (Anura: Pipidae). *J Morphol* **214**, 1–41.

Tsai HP, Holliday CM (2011) Ontogeny of the alligator cartilago transiliens and its significance for sauropsid jaw muscle evolution. *PLoS One* **6**, e24935.

Van Dijk DE (2002) Longitudinal sliding articulations in pipid frogs. *S Afr J Sci* **98**, 555–556.

Wheeler GN, Brändli AW (2009) Simple vertebrate models for chemical genetics and drug discovery screens: lessons from zebrafish and *Xenopus*. *Dev Dyn* **238**, 1287–1308.

Whiting HP (1961) Pelvic girdle in amphibian locomotion. *Symp Zool Soc Lond* **5**, 43–57.

Ziermann JM, Diogo R (2014) Cranial muscle development in frogs with different developmental modes: direct development versus biphasic development. *J Morphol* **275**, 398–413.

Ziermann JM, Olsson L (2007) Patterns of spatial and temporal cranial muscle development in the African Clawed Frog, *Xenopus laevis* (Anura: Pipidae). *J Morphol* **268**, 791–804.

Supporting Information

Additional Supporting Information may be found in the online version of this article:

Fig. S1. Interactive 3D PDF of the digitally segmented skeleton of *Xenopus laevis.*

Fig. S2. Interactive 3D PDF of the digitally segmented musculature of *Xenopus laevis*; with the exception of m. longissimus dorsi, only right side muscles are shown.

Fig. S3. Interactive 3D PDF of the digitally segmented nervous system of *Xenopus laevis.*

Fig. S4. Interactive 3D PDF of the digitally segmented digestive, urogenital and respiratory systems of *Xenopus laevis.*

© 2017 Anatomical Society